Intrinsic interval timing, not temporal prediction, underlies ramping dynamics in visual and parietal cortex

Yicong Huang[1], Ali Shamsnia[2], Mengze Chen [2], Shuang Wu[2], Tim Stamm[2], Sophie Medico[2], Farzaneh Najafi[2#]

[1] Wallace H Coulter Department of Biomedical Engineering, Georgia Institute of Technology and Emory University
[2] School of Biological Sciences, Georgia Institute of Technology

Corresponding author: fnajafi3@gatech.edu

Abstract

Neural activity following regular sensory events can reflect either elapsed time since the previous event (temporal signaling) or temporal predictions and prediction errors about the next event (temporal predictive processing). These mechanisms are often confounded, yet dissociating them is essential for understanding neural circuit computations. We addressed this by performing two-photon calcium imaging from distinct cell types (excitatory, VIP and SST) in layer 2/3 of visual and posterior parietal cortex (PPC), while awake mice passively viewed audio-visual stimuli under temporal contexts with different inter-stimulus interval (ISI) distributions. Computational modeling revealed distinct functional clusters of neurons, including stimulus-activated (ramp-down) and stimulus-inhibited (ramp-up) categories, with distinct kinetics and area/cell-type biases.

Importantly, all functional clusters were invariant to temporal predictability, shifted immediately when temporal statistics changed, and were identical between naive and experienced mice. Population decoding revealed that clusters with heterogeneous kinetics differed in how well they represented interval information, such that together they tiled elapsed time and produced a distributed, learning-independent population code for time. These results provide strong evidence against temporal predictive processing in V1/PPC under passive conditions and instead demonstrate intrinsic coding of interval timing, redefining the mechanistic origin of ramping and omission-related activity in sensory cortex. We discuss how these dynamics align with stimulus-reset attractor frameworks, and propose that temporal predictive processing is more likely implemented in other circuits or recruited in V1/PPC during task-engaged behavior.

Introduction

The brain continuously encodes the passage of time and generates expectations about when future events will occur. These temporal computations are critical for perception, motor control, and learning, yet their neural underpinnings remain debated.

Neural activity between sensory events may reflect two distinct processes: elapsed-time signaling, which encodes the duration since the previous event, and temporal predictive processing, which represents the expected timing of the next event. These processes unfold concurrently; hence, it is often difficult to determine whether neural responses in a given circuit reflect temporal tracking or predictive processing mechanisms.

Temporal signaling, the encoding of elapsed time, is achieved through multiple mechanisms (Coull et al., 2011; Tsao et al., 2022), such as ramping (gradual changes in neural activity) (Cueva et al., 2020; Narayanan, 2016), sequential activation of neurons (S. Zhou et al., 2020), and population trajectories, where activity patterns of recurrently-connected neurons evolve through a high-dimensional state space, with each state carrying information about elapsed time (Machens et al., 2010; Mante et al., 2013; Murray et al., 2014; Paton & Buonomano, 2018; Wang et al., 2018).

Synaptic mechanisms, such as short-term plasticity that modulate how neurons respond to inputs over time (Feldman, 2012; Laje & Buonomano, 2013), together with variability in intrinsic time constants, generate heterogeneous dynamics across the population. This diversity acts as a temporal basis set: overlapping dynamics tile different segments of an interval, allowing downstream circuits to reconstruct elapsed time from distributed activity. Such population-level coding has been observed across cortical, striatal, hippocampal, and cerebellar circuits (Bernacchia et al., 2011; Buonomano & Maass, 2009; Chabrol et al., 2015; Garcia-Garcia et al., 2024; Herzfeld & Lisberger, 2025; MacDonald et al., 2011; Matell et al., 2003; Medina & Mauk, 2000; Mello et al., 2015; Pastalkova et al., 2008).

In the cortex, both sensory and associative areas demonstrate temporal processing. For example, neurons in the posterior parietal cortex (PPC) contribute to interval production and categorization (Bueti & Walsh, 2009; Hayashi et al., 2015; Janssen & Shadlen, 2005; Leon & Shadlen, 2003; Schneider & Ghose, 2012), and neurons in frontal/prefrontal cortices demonstrate population trajectories that flexibly “scale” with the demanded interval length (Kim et al., 2013; Wang et al., 2018; Xu et al., 2014). Primary sensory cortices also show timing signatures when stimuli are predictable: neurons in primary visual and auditory cortex “remember” recent intervals, through stimulus-evoked state shifts that depend on short-term depression/facilitation (Gavornik & Bear, 2014; Jaramillo & Zador, 2011).

Predictive-processing, on the other hand, suggests that cortical areas contain internal models of the world, leading to predictions that are compared with sensory inputs. In case of a mismatch, prediction-error (PE) signals are generated, which then update the internal model (Aizenbud et al., 2025; Friston & Kiebel, 2009; Keller & Mrsic-Flogel, 2018; Rao & Ballard, 1999; Schneider et al., 2018). This canonical computation has been identified across many brain

regions and species, and applies to both the identity and the timing of sensory inputs; i.e. what and when a stimulus will occur (Aizenbud et al., 2025). Both the primary visual cortex (V1) and the PPC are involved in predictive processing (Aizenbud et al., 2025; Fiser et al., 2016; Furutachi et al., 2024; Garrett, Groblewski, Piet, Ollerenshaw, Najafi, et al., 2023; Garrett et al., 2020; Hamm et al., 2021; Najafi et al., 2025; Van Derveer et al., 2023; Z. C. Zhou et al., 2020).

Predictive processing, on the other hand, suggests that cortical areas contain internal models of the world, which generate predictions that are compared with sensory inputs. When a mismatch occurs, prediction error (PE) signals are generated to update the internal model (Aizenbud et al., 2025; Friston & Kiebel, 2009; Keller & Mrsic-Flogel, 2018; Rao & Ballard, 1999). This canonical computation has been identified across many brain regions and species, and applies to both the identity and the timing of sensory inputs—that is, *what* and *when* a stimulus will occur (Aizenbud et al., 2025). Multiple cortical areas—including primary visual cortex (V1) and posterior parietal cortex (PPC)—have been implicated in predictive processing (Aizenbud et al., 2025; Fiser et al., 2016; Furutachi et al., 2024; Garrett, Groblewski, Piet, Ollerenshaw, Najafi, et al., 2023; Garrett et al., 2020; Hamm et al., 2021; Najafi et al., 2025; Van Derveer et al., 2023; Z. C. Zhou et al., 2020).

Cell-type-specific studies demonstrate a key role for inhibitory neurons—particularly VIP and SST interneurons—in predictive processing (VIP: vasoactive intestinal peptide; SST: somatostatin). VIP neurons—in primary and higher visual areas—respond to the change (G. Bastos et al., 2023; Furutachi et al., 2024) or omission (Furutachi et al., 2024; Garrett, Groblewski, Piet, Ollerenshaw, Yavorska, et al., 2023; Garrett et al., 2020; Najafi et al., 2025; Nitzan & Buzsáki, 2025) of expected visual stimuli. SST interneurons, in the PPC, include a molecularly defined subset that carries an error-correction signal during navigation tasks (Green et al., 2023). Computational modelling and circuit dissection suggest that VIP–SST–Excitatory disinhibitory circuit can give rise to PE neurons (Hertäg & Sprekeler, 2020; Keller et al., 2020).

In temporal processing, too, inhibitory neurons play a role: SST interneurons are required for sequential population activity in both motor (Adler et al., 2019) and prefrontal cortex (Abbas et al., 2018). Particularly relevant to the present study is the ramping activity—observed in most VIP and some excitatory neurons—prior to an *expected* stimulus. Importantly, this ramp continues even further, when that stimulus is omitted (Garrett, Groblewski, Piet, Ollerenshaw, Najafi, et al., 2023; Garrett et al., 2020; Najafi et al., 2025).

Disambiguating temporal signaling from predictive processing. Temporal processing and temporal predictive processing can co-occur; however, their computational requirements differ. Predictive processing relies on learned internal models and therefore suggests that prediction signals should strengthen with experience. Temporal signaling, in contrast, can arise intrinsically from recurrent or synaptic dynamics and should be present even in naïve animals exposed to irregular stimulus statistics.

Many experimental paradigms entangle these processes. Regularly repeated stimuli simultaneously provide temporal signals and high predictability, making it difficult to attribute neural responses—such as ramping before a predictable event or activity after an unexpected

sensory omission—to one mechanism or the other. Disambiguating the two is essential for assigning correct computational roles to specific circuits and cell types.

Present Study. We devised a three-stage paradigm in awake, head-fixed mice to tease apart temporal predictive processing and temporal signaling while performing two-photon calcium imaging of layer 2/3 excitatory, VIP, and SST neurons in V1 and PPC. Across all experiments, mice passively viewed repeating audio-visual stimuli (0.2 s), separated by inter-stimulus intervals (ISIs) that varied according to the paradigm design.

1. Random ISI sessions: naïve mice received stimuli at uniformly distributed inter-stimulus intervals (ISIs, 0.5–2.5 s). High temporal variability minimizes timing predictions; interval-dependent activity is therefore primarily attributed to temporal processing.

2. Fixed/Jittered ISI sessions: blocks of trials with fixed ISI (1.5 s)—hence fully predictable—alternated with blocks of jittered ISIs (0.5-2.5 s). Both blocks included occasional deviant ISIs (0.5 or 2.5 s: shorter or longer than expected), representing temporal prediction errors. Predictive processing predicts weaker anticipatory and prediction-error signals under jitter, whereas temporal processing should encode interval length regardless of variability.

3. Short/Long ISI blocks: mice experienced trial blocks alternating between 1-s or 2-s fixed ISIs, allowing us to test adaptation of timing signals, and to probe whether block transitions elicit prediction-error responses.

Results. Across all three paradigms, neural dynamics in V1 and PPC were best accounted for by temporal signaling rather than predictive processing. Neurons clustered into two major families—stimulus-activated and stimulus-inhibited/ramp-up—with subtypes defined by distinct rise and decay kinetics. Their activity shifted immediately at transitions between short and long blocks, inconsistent with gradual prediction updating. Deviant intervals in fixed versus jittered blocks elicited no differential responses, and the same functional clusters were present even in naïve animals exposed to random intervals. Decoding analyses revealed that heterogeneous kinetics across neurons tiled elapsed time, generating a distributed population code for interval timing. Together, these findings establish that passive temporal dynamics in V1 and PPC reflect intrinsic elapsed-time signaling, not temporal predictive processing.

Significance. These results resolve longstanding ambiguities by showing that ramping dynamics previously interpreted as predictive signals in visual cortex instead reflect intrinsic temporal processing. More broadly, they underscore the importance of incorporating carefully designed jittered paradigms before attributing ramping or omission-related activity to prediction or prediction-error signals. Key next steps are to: (1) dissect the cellular and synaptic mechanisms underlying intrinsic temporal codes in cortex; (2) identify the circuits that implement temporal predictive processing during passive perception; and (3) determine whether, in perceptual decision tasks, PPC/V1 dynamics remain signatures of elapsed time or shift toward predictive coding.

Results

Paradigms to disentangle temporal signaling from temporal predictive processing

Neural signals during the interval between two events could reflect either of two processes (**Fig. 1A**): **(1)** the elapsed time since the previous event (temporal signaling), or **(2)** the expected timing of the next event (temporal predictive processing). These processes unfold concurrently, making it difficult to determine which function a neural circuit represents. Disentangling them is essential, because they rely on distinct underlying computations, and failing to do so risks misinterpreting circuit function.

To address this, we designed three paradigms to separate temporal signaling from predictive processing. Awake, head-fixed mice passively viewed a stream of repeating audio-visual stimuli (0.2 s), separated by an inter-stimulus interval (ISI; 0.5–2.5 s) (**Fig. 1B**; ISI includes gray screen and no auditory stimulus). Each stimulus consisted of a simultaneous auditory tone (11 kHz) and visual grating (whole-field static black/white stripes). Two-photon calcium imaging, via GCaMP8f (Zhang et al., 2023), was performed from the primary visual cortex (V1) and the posterior parietal cortex (PPC). Layer 2/3 excitatory neurons and VIP interneurons were simultaneously imaged in one cohort, and SST interneurons were imaged in a separate cohort (VIP-Cre;Ai14 mice and SST-Cre mice injected with GCaMP8f; **Fig. 1C–E**).

The three paradigms were short/long, fixed/jittered, and random sessions (**Fig. 1F–H**).

- In short/long sessions, two block types alternated (50 trials each): ISI was fixed at 1 s in short blocks and 2 s in long blocks (**Fig. 1F**).
- In fixed/jittered sessions, two block types alternated (200 trials each): ISI was fixed at 1.5 s in fixed blocks, and randomly drawn from a uniform 0.5–2.5 s distribution in jittered blocks (**Fig. 1G**). Each block also contained 4% deviant ISIs (short deviant: 0.5 s; long deviant: 2.5 s). Deviants carried much higher surprisal in fixed blocks, since in jittered blocks they lay within the expected ISI range.
- In random sessions, all ISIs were independently drawn from the same uniform 0.5–2.5 s distribution (**Fig. 1H**).

Importantly, naïve mice were first exposed to the random sessions, before experiencing the short/long and fixed/jittered paradigms. This design allowed us to examine neural responses to random intervals in animals without prior exposure to our stimuli.

V1 and PPC neurons demonstrate stimulus-activated and ramping dynamics to repeating audio-visual stimuli

We measured the response of excitatory, VIP, and SST neurons in V1 and PPC (**Supp Fig. 1**) during passive audio-visual stimulation, using two-photon calcium imaging. Neurons in both areas showed diverse response profiles (**Fig. 2A**), hence we clustered them into functional subtypes (**Fig. 1I**).

To perform clustering, we first modeled single-neuron responses using a generalized linear model (GLM). We then fit an ex-Gaussian temporal receptive field (TRF) model (Affan et al., 2024; Cao et al., 2024; Bright et al., 2020; Cruzado et al. 2020) to the GLM-derived stimulus kernel to extract response parameters such as ramp speed, and temporal width (**Fig. 6C,E; Supp Fig. 3**). These parameters were then clustered using k-means to define functional subtypes.

Two broad clusters emerged: stimulus-inhibited (**Fig. 2A-C**; rows 1-2) and stimulus-activated (**Fig. 2A-C**; rows 3-5) neurons. Stimulus-inhibited responses typically evolved into a gradual ramp-up, whereas stimulus-activated responses evolved into a gradual ramp-down. Accordingly, we also refer to these clusters as ramp-up and ramp-down neurons, respectively. Both clusters contained subtypes with distinct response dynamics: stimulus-activated neurons ranged from fast/narrow to slow/broad responses (**Fig. 2B**; rows 3-5), while stimulus-inhibited neurons differed in ramp onset and amplitude (**Fig. 2B**; rows 1-2).

Stimulus-activated clusters with slow/broad peaks were more frequent in PPC (**Fig. 2B**; rows 4-5; 25% V1 neurons vs. 34% PPC neurons), whereas V1 contained more stimulus-inhibited ramp-up clusters (**Fig. 2B**; rows 1-2; 40% V1 neurons vs. 29% PPC neurons). The prevalence of slow stimulus-driven clusters in PPC aligns with the role of higher-order associative areas in perception (Avanzini et al., 2016). The presence of ramp-up clusters in PPC confirms and extends previous reports of ramping neurons in V1 and higher visual areas (Garrett et al., 2020; Najafi et al., 2025).

Excitatory and inhibitory subtypes contributed to all clusters, but to varying degrees. SST neurons were most prevalent in stimulus-activated clusters (Garrett, Groblewski, Piet, Ollerenshaw, Najafi, et al., 2023) (**Fig. 2C,D**). In contrast, a substantial fraction of VIP and excitatory neurons was stimulus-inhibited (Garrett, Groblewski, Piet, Ollerenshaw, Najafi, et al., 2023) (**Fig. 2C,D**).

Interval transitions evoke immediate, non-gradual neural response changes

To study how V1/PPC responses encode distinct intervals, we compared neural activity between short- and long-ISI blocks in the short/long paradigm (**Fig. 1F**; short ISI: 1 s; long ISI: 2 s). All clusters showed distinct activity patterns between the two blocks (**Fig. 3A-C**; blue: short block; green: long block). Stimulus-activated clusters exhibited smaller response amplitudes during the short-ISI block (**Fig. 3B**; rows 3-5). Stimulus-inhibited clusters differed in ramp kinematics across short/long blocks (**Fig. 3B**; rows 1-2). Notably, clear ramps were observed in the long block, whereas the same neurons appeared much less responsive during the short block (**Fig. 3B**; rows 1-2).

We next examined how responses adapted following block transitions (**Fig. 3D-F**). Surprisingly, all clusters showed immediate response changes. During short-to-long transitions, stimulus-activated clusters increased response amplitude on the very first long-ISI trial (**Fig. 3E,F left**; rows 3-4)., while stimulus-inhibited clusters exhibited much more pronounced ramps, already evident in the first long-ISI (**Fig. 3E,F left**; rows 1-2).. The opposite effects were observed during

long-to-short transitions, with stimulus-activated clusters decreasing in amplitude and stimulus-inhibited clusters showing attenuated ramps (**Fig. 3E,F right**).

To quantify these dynamics, we measured response magnitude across three epochs: immediately before a block transition, immediately after, and late within the block (Pre, Early, Late, respectively; **Fig. 3F**). This analysis confirmed that neural responses across all clusters changed immediately after interval transitions and remained generally stable within each block (**Fig. 3F**).

Short/long interval transitions are inconsistent with temporal predictive processing

The predictive processing hypothesis posits that a change in interval at block transitions should generate a temporal prediction error, which would gradually diminish within a block as new temporal predictions emerge. Our short/long-session results do not support this.

<u>Short-to-long transitions:</u> Stimulus-inhibited clusters exhibited activity changes at the time of the unexpectedly omitted stimulus in the first long ISI (**Fig. 3E left**; yellow line), which could superficially resemble a prediction-error signal. However, the magnitude and timing of ramps remained stable across subsequent long-interval trials (**Fig. 3E,F left**).

<u>Long-to-short transitions:</u> Stimulus-inhibited neurons did not respond to the first short-ISI trial, and stimulus-activated neurons showed reduced response amplitude (**Fig. 3E right**; redline). Also, no further changes were observed during subsequent trials after the transition (**Fig. 3E right**).

Taken together, the lack of a clear prediction-error response at the time of unexpected events (**Fig. 3E**; yellow and red lines), combined with immediate rather than gradual changes after block transitions, argue against the temporal predictive processing hypothesis.

Fixed/jittered blocks confirm absence of temporal predictions and errors in V1 and PPC

While our short/long-session results do not support temporal predictions or prediction errors, alternative explanations could be considered. One possibility is that neurons encode only long-ISI prediction errors, since some activity changes coincided with stimulus omissions. Another is that the absence of change after short-to-long transitions reflects co-occurring signals within the same neurons—prediction signals that gradually increase and prediction-error signals that gradually decrease—effectively canceling each other. Finally, for long-to-short transitions, a high learning rate could allow predictions to be updated in a single trial, explaining the absence of gradual adaptation.

To test these scenarios more directly, we ran fixed/jittered-block sessions (**Fig. 1G**). Fixed blocks consisted of constant ISIs (1.5 s) with occasional unexpected short or long intervals (deviants: 0.5 s and 2.5 s). In jittered blocks, ISIs were drawn from a uniform 0.5–2.5 s distribution, so the same 0.5 s and 2.5 s intervals were expected. Predictive processing therefore predicts stronger prediction-error responses to deviant ISIs in fixed compared to jittered blocks, as well as stronger prediction signals in fixed blocks due to temporal regularity.

Surprisingly, and in clear contrast to predictive-processing predictions, responses to deviant ISIs were indistinguishable between fixed and jittered blocks, for both short and long deviants (**Fig. 4A,E**, for long and short deviants, respectively; red: fixed, blue: jittered). This key result provides strong evidence against temporal prediction-error coding in PPC or V1 during passive audiovisual stimulation. Ramp-up neurons likewise showed no difference across fixed and jittered contexts (**Fig. 4A,E**; rows 1-2; see ramps prior to stimulus at t=0), inconsistent with ramping activity representing temporal prediction signals, which should have weakened under jitter.

A potential counterargument is that both block types shared the same mean ISI (1.5 s), so average ramp dynamics might overlap despite differences in trial-to-trial variability. To address this, we computed a single-trial modulation index to quantify responses to unexpected events—specifically, stimulus omissions during long deviants and unexpected stimulus deliveries during short deviants (including the stimulus immediately following a long deviant)—and compared its distribution between the two block types (**Supp Fig. 2**). However, we found no differences between fixed and jittered blocks, whether in response mean or variance, for either long or short deviants (**Supp. Fig. 2**; mean comparison: two-tailed Mann–Whitney U test; variance comparison: two-tailed Levene's test; significance threshold: $p < 0.05$).

To test whether subtle differences might be obscured in mean responses, we trained a linear decoder to classify fixed versus jittered trials based on activity around deviant ISIs (**Fig. 4B**). Decoder performance remained at chance, providing further evidence that responses to deviants were indistinguishable between fixed and jittered conditions (**Fig. 4B,F**: long and short deviants, respectively; purple: data, gray: shuffled control).

Finally, we performed principal component analysis (PCA) to examine how population trajectories change during unexpected events in both fixed and jittered contexts (**Fig. 4C,G**: population averages; **Fig. 4D,H**: top 3 principal components; yellow line/box: unexpected stimulus omission during long deviants; red line/box: unexpected stimulus delivery after a deviant ISI). In both contexts, stimulus onset drove trajectories to an evoked state, which then gradually relaxed back (**Fig. 4D**, gray: pre-deviant stimulus).

Importantly, unexpected omissions (**Fig. 4D**, top; yellow) did not perturb the trajectory, which continued in state space until the next stimulus (**Fig. 4D**, red: late stimulus), closely resembling the jittered trajectory (**Fig. 4D**, bottom). The late stimulus following a deviant, despite its unexpected timing, produced a trajectory similar to that evoked by a predictable stimulus (**Fig. 4D**, gray vs. red), and this similarity was observed in both fixed and jittered conditions (**Fig. 4D**: PCA; **Fig. 4C**: population averages). A similar lack of difference was observed for short deviants: in both fixed and jittered contexts, the post-deviant stimulus ("early stimulus," **Fig. 4G,H**; red) pushed trajectories into an evoked state. Compared to the stimulus before the short deviant (**Fig. 4H**; gray), this early stimulus produced a smaller trajectory change, consistent with the reduced response amplitudes in short versus jittered blocks (**Fig. 3B**).

Neural ramps are intrinsic, encoding elapsed time from the previous event

While the similar response means and variances between fixed and jittered blocks argue against ramps reflecting temporal predictions, one could argue instead that these neurons encode predictions about the *stimulus itself* rather than its timing—specifically, the prediction that each stimulus will be followed by another. In this view, because mice were exposed to repeating stimuli for many days, such stimulus predictions would persist in jittered blocks and would be equally strong in fixed blocks.

To directly test this alternative, we turned to entirely naïve mice that had never experienced our paradigms and presented them with repeating stimuli at random ISIs. On their very first day of exposure, both temporal and stimulus predictions should be absent.

We observed the same neuronal clusters—stimulus-activated and inhibited—even in naïve mice (**Fig. 5**). Strikingly, ramp-up neurons were already present from the very first session (**Fig. 5C**). To address the possibility that rapid predictions might emerge within the first day, we compared neural responses between the first 100 and last 100 stimuli of day 1, but again found no difference (**Fig. 5D**; black: first epoch; blue: last epoch). Finally, the prevalence of clusters remained generally stable across days (**Fig. 5E**).

Across all paradigms, our evidence argues that neural responses—and particularly the ramp-ups—are not related to temporal prediction signals. A key question, then, is what signal these neurons, through their ramps and different kinetics, actually encode. We hypothesized that they represent elapsed-time signals. To test this, we binned the random intervals and examined how responses evolved (**Fig. 5F**). Stimulus-activated responses were similar across bins, but their relaxation (ramp-down) was truncated when the next stimulus occurred early (**Fig. 5F;** rows 4-5; shorter bins: green shades) and extended further when the next stimulus was delayed (**Fig. 5F**; rows 4-5; longer bins: orange/pink). Likewise, the ramp-up in stimulus-inhibited clusters was interrupted, if a stimulus occurred early, whereas it continued further when the next stimulus was delayed (**Fig. 5F**; rows 1-3; shorter bins: green shades; longer bins: orange/pink). Thus, neural responses across ISI bins appeared as different snapshots of the same underlying dynamic, interrupted and reset whenever the next stimulus arrived (**Fig. 5F**).

Population trajectory analysis confirmed this view (**Fig. 5H**, top 3 principal components): trajectories followed a common path across all intervals, simply evolving further along the same trajectory until reset by the next stimulus (**Fig. 5H**; random ISIs divided into 10 bins; trajectories start at stimulus onset and end at the mean ISI bin). Together, these results indicate that V1 and PPC dynamics during the interval reflect intrinsic relaxation processes reset by each stimulus, rather than adaptation or prediction-error mechanisms.

Heterogeneous rise/decay kinetics enable population coding of time

Our results so far demonstrate that responses following a stimulus reflect the unfolding of intrinsic cortical dynamics, thereby enabling elapsed-time signaling. We next tested this directly using a time-decoding analysis. We reasoned that the diversity of dynamics across neurons should generate a population code for time: neurons with different rise and decay kinetics would have distinct temporal preferences, and together they would span a wide range of intervals.

To assess this, we trained a decoder to discriminate pairs of time bins based on population activity within each cluster (**Fig. 6B**; binary linear SVM trained on long-block data from the short/long sessions: **Fig. 6A**). Neurons within each cluster were subsampled to the same count to allow unbiased cross-cluster comparison. All clusters carried information about elapsed time, but their decoding profiles differed systematically (**Fig. 6B**; chance at 50%). Stimulus-activated clusters decoded short intervals more accurately, with high initial accuracy that declined over time (**Fig. 6B**; rows 3-5). In contrast, stimulus-inhibited clusters showed stable decoding throughout the interval, with a small increase in accuracy near the end, consistent with their ramp-up dynamics (**Fig. 6B**; rows 1-2).

To understand how response kinematics shape these profiles, we compared parameters of the temporal receptive field model across clusters (**Fig. 6C,E**). A clear pattern emerged: clusters with faster and narrower responses supported higher temporal precision (**Fig. 6D,E**; green; cyan), whereas clusters with slower and broader responses provided more stable decoding (**Fig. 6D,E**; blue; orange; red).

Altogether, these findings support a simple mechanistic model: stimulus onset resets the population into an evoked state that then relaxes toward baseline. Both the rise into the evoked state and the decay back vary across neurons. This diversity in response kinetics enables the population to represent elapsed time across multiple scales. Accordingly, changes in neural responses across ISIs reflect sampling different phases of a shared trajectory, rather than adaptive or predictive mechanisms.

Discussion

Results summary

During passive presentation of repeated audiovisual stimuli, V1 and PPC neurons clustered into two broad families: stimulus-activated neurons and stimulus-inhibited (ramp-up) neurons. Within each family, subtypes were distinguished by their rise and decay kinetics, ranging from fast to slow temporal profiles. Responses showed immediate changes at ISI transitions (Fig. x), with no deviant-specific effects in fixed versus jittered blocks (Fig. x), and the same clusters were present in naïve mice during fully random ISIs (Fig. x). Decoding analysis revealed that neural clusters encoded interval timing information, with each cluster's interval preference determined by the rise and decay kinetics of its neurons (Fig. x). Together, these findings indicate an intrinsic, distributed code for elapsed time in V1 and PPC during passive behavior, without invoking temporal predictive processing or learning mechanisms.

Ramps and omissions reflect intrinsic timing, rather than predictions or prediction errors

Temporal predictive processing refers to the brain's ability to predict the timing of upcoming sensory events and generate prediction errors when these expectations are violated. A common approach for studying this brain function is to present stimuli at regular intervals. However, in such paradigms, temporal prediction signals often overlap with elapsed-time signals, which

reflect the time since the previous stimulus. This overlap makes it difficult to determine whether neural activity reflects prediction or simple temporal tracking.

Our fixed/jittered paradigm with deviant ISIs, together with the random-ISI paradigm in naïve mice, provide a powerful tool to separate elapsed-time signaling from temporal predictive processing. Without these paradigms, neural responses to long-ISI deviants (omissions) could be mistakenly interpreted as temporal prediction errors, and ramping signals as temporal predictions.

The predictive processing framework suggests that: **1)** Deviant ISIs should generate stronger prediction errors in fixed blocks compared to jittered blocks, and temporal predictions should be stronger in fixed blocks. **2)** Naïve mice exposed for the first time to random intervals should not exhibit temporal predictions. **3)** In short/long-ISI sessions, temporal prediction errors should arise at block transitions, leading to gradual within-block adaptation and updating of predictions.

Our data contradict all of these predictions: **1)** We observed no differences between fixed and jittered blocks, for either standard or deviant ISIs (Fig. x). **2)** Neural subtypes, including ramping clusters, were indistinguishable between naïve and experienced mice (Fig. x). **3)** No gradual adaptation followed block transitions; instead, responses changed immediately (Fig. x).

Together, these results demonstrate that the ramping and omission responses observed in V1 and PPC, during passive stimulation, reflect intrinsic elapsed-time signaling, rather than temporal predictive processing.

Interval representation emerges from stimulus-reset attractor dynamics

Our results can be understood within an attractor-dynamics framework (Hennequin et al., 2018; Rajan et al., 2010; X.-J. Wang, 2008), in which each stimulus pushes neurons from baseline into a transient evoked state, after which activity relaxes back toward baseline. In this view, responses differ across interval lengths not because of trial-by-trial learning, but because the same intrinsic trajectory is **reset** and restarted at different points in its cycle.

This framework naturally accounts for our key findings: (i) the immediate changes in neural responses at block transitions (Fig. x) without invoking trial-by-trial learning; (ii) identical responses between fixed and jittered ISI contexts (Fig. x), despite lower predictability in the jittered case and weaker deviant responses; and (iii) the presence of the same neural clusters in both naïve and experienced mice (Fig. x).

Importantly, this view situates our results within a broader attractor literature. Stimulus-reset attractor dynamics have been linked to variability quenching at onset (Churchland et al., 2010; Hennequin et al., 2018) and to persistent activity in working-memory and decision circuits (Inagaki et al., 2019; Wang et al., 2023; X. J. Wang, 2008). Our findings extend this framework to interval signaling: stimulus onsets place V1/PPC populations onto reproducible evoked trajectories whose cluster-specific kinetics tile elapsed time, thereby yielding a learning-independent population code for interval duration (Murray et al., 2014; Paton & Buonomano, 2018).

Revisiting visual omission responses in passive paradigms

Previous paradigms using random omissions of expected visual inputs reported omission responses in excitatory and VIP neurons of visual cortex, which were interpreted as temporal expectation (Nitzan & Buzsáki, 2025) and/or prediction-error signals (Fiser et al., 2016; Furutachi et al., 2024; Garrett, Groblewski, Piet, Ollerenshaw, Najafi, et al., 2023; Garrett et al., 2020; Najafi et al., 2025). Our findings demonstrate instead that these so-called omission responses reflect neither expectation nor prediction error, but rather the intrinsic unfolding of stimulus-evoked activity and its relaxation back toward baseline. Moreover, although behavioral variables may co-vary with omissions [Najafi, 2025], our results show that they are not the cause of these responses—because, fundamentally, there is no separate "omission response," only the continuation of intrinsic dynamics.

A recent study (Nitzan & Buzsáki, 2025) is specifically relevant to our findings. By performing an elegant reanalysis of large-scale datasets from the Allen Institute, the authors concluded that visual cortex neurons do not encode prediction errors, and hence, suggested that omission responses may reflect temporal expectation or rebound activity. Our study builds on these insights with a dedicated experimental paradigm specifically designed to disentangle elapsed-time signaling from predictive processing. By systematically comparing fixed/jittered intervals, and naïve/experienced mice, we confirm that V1 responses are not prediction errors and further demonstrate that they do not reflect temporal predictions either. Instead, the ramping dynamics in visual cortex arise from intrinsic elapsed-time signaling, revealed only through carefully controlled paradigms.

Possible sites of temporal predictive processing during visual perception

A pressing question raised by our findings is where in the brain temporal predictive processing during passive visual inputs is implemented (Coull et al., 2011). Hippocampal neurons—and subcortical regions such as the thalamic medial geniculate nucleus—have been suggested to carry temporal prediction-error signals, since, compared to the gradual ramps observed in visual cortex, they exhibit steeper responses to visual omissions (Nitzan & Buzsáki, 2025).

Another potential candidate is the cerebellum. Numerous studies have established its role in encoding timing and error signals during sensorimotor behavior (Boven et al., 2025; Gao et al., 2018 Li 2018; Garcia-Garcia et al., 2024; Giovannucci et al., 2017; Herzfeld & Lisberger, 2025; Medina & Mauk, 2000; Najafi & Medina, 2013; O'Reilly et al., 2008; Ohmae et al., 2017; Shadmehr et al., 2010; Suvrathan et al., 2016). Fewer studies have examined the cerebellum's role during passive stimulation (Najafi et al., 2014), but evidence shows that the cerebellum is active following unexpected omissions of passive somatosensory stimuli (Tesche & Karhu, 2000) and is necessary for detecting temporal mismatches during passive auditory inputs (Moberget et al., 2008). With respect to visual inputs, the cerebellum encodes repeated visual stimuli and their omissions during motor behavior (Kameda et al., 2019), but its role during passive visual perception remains to be determined.

Other candidate regions for temporal predictive processing include the basal ganglia (Kameda et al., 2019; Matell et al., 2003; Mello et al., 2015) and the prefrontal cortex (Kim et al., 2013; Wang et al., 2018; Xu et al., 2014), alongside the auditory cortex, whose role in auditory temporal predictive processing is well established (Jaramillo & Zador, 2011; Schneider et al., 2018; Yaron et al., 2024).

V1/PPC, too, may reflect temporal prediction signals but in active perceptual paradigms where animals need to attend to stimuli to receive reward. Human EEG studies support this view: anticipatory signals were absent during passive rhythmic streams but emerged when subjects prepared for action (Breska & Deouell). Future studies using paradigms similar to ours, but including active perceptual or behavioral contexts, will be critical for determining whether V1 and PPC dynamics shift from elapsed-time coding toward predictive processing. Also, several animal studies have reported predictive and error signals in cortical areas when sensory events are behaviorally relevant (Chubykin et al., 2013; Cole et al., 2024; Hockley et al., 2025; Jordan & Keller, 2020; Najafi et al., 2020; Shuler & Bear, 2006). This implies that task engagement may be necessary to recruit temporal predictive processing in these circuits.

Diverse neuronal dynamics provide a distributed code for time

Neurons in V1 and PPC showed heterogeneous dynamics after stimulus presentation: both the rise into the evoked state and the decay back to baseline varied across cells. Some stabilized at baseline after recovery (Fig. x), consistent with fixed-point attractors, whereas most gradually drifted over time (Fig. x), consistent with manifold-like dynamics in which the attractor landscape is shallow enough to allow slow evolution in state space rather than collapse to a single fixed point. This heterogeneity aligns with reservoir models of diverse timescales, where variable neuronal kinetics create overlapping trajectories that together form a distributed population code for elapsed time (Bernacchia et al., 2011; Buonomano & Maass, 2009; Murray et al., 2014; Paton & Buonomano, 2018; Wang et al., 2018).

Evidence for such diverse (Affan et al., 2025) timescales extends across brain systems: in the cerebellum, granule cells provide heterogeneous temporal kernels important for interval learning (Barri et al., 2022; Garcia-Garcia et al., 2024; Medina & Mauk, 2000); in the striatum, medium spiny neurons exhibit sequential dynamics that tile time over seconds (Matell et al., 2003; Mello et al., 2015); and in the hippocampus, “time cells” fire at distinct delays from an event, collectively spanning behavioral intervals (MacDonald et al., 2011; Pastalkova et al., 2008).

The diversity of rise and decay dynamics effectively provides a set of temporal filters in which each neuron is tuned to a different portion of the interval. In this sense, the population acts like a basis set: overlapping response profiles that can be flexibly combined downstream to reconstruct elapsed time. Such an organization enhances robustness to noise, since time is represented redundantly, and allows different circuits to emphasize narrow or broad signals depending on task demands. This framework parallels basis-function models of time in recurrent networks and supports the view that elapsed time is encoded through a distributed population code rather than by a single dedicated mechanism (Buonomano & Maass, 2009; Laje &

Buonomano, 2013; Paton & Buonomano, 2018).

Contrast with temporal scaling models. Our findings complement but also diverge from the temporal scaling framework described in behaving animals and recurrent network models (Wang et al., 2018). Temporal scaling emphasizes that the same population trajectory can be flexibly stretched or compressed in time, with trajectory speed adjusted to represent short versus long intervals.

By contrast, our data show that passive interval coding in V1 and PPC does not arise from scaling a common trajectory: responses to short and long intervals were not scaled versions of one another. Instead, each neuron contributes a fixed trajectory defined by its own timescale, and stimuli presented at different intervals reset these trajectories at different phases. Thus, while both frameworks support the idea that time is encoded in evolving population activity rather than by a dedicated clock, our results point to a distributed tiling of intrinsic trajectories rather than flexible rescaling of a single one.

Cell-type-specific mechanisms underlying heterogeneous neural dynamics

While all cell types contributed to each functional cluster, there were notable cell-type-specific differences: SST cells were more dominant in fast stimulus-excited/inhibited clusters, while VIP and excitatory neurons were more prominent in ramp-up/down clusters.

These findings align with the functional roles of different cell types in shaping the temporal dynamics of neural responses. SST cells, which receive strong visual input in V1, mediate rapid inhibitory transients, shaping fast temporal dynamics of stimulus-driven activity. This matches the narrow responses observed in our stimulus-excited/inhibited clusters (Shin & Adesnik, 2021; Tremblay et al., 2016). In contrast, VIP interneurons and excitatory neurons show slower dynamics, as seen in the ramp-up/ramp-down clusters. VIP interneurons—activated by behavioral state, reinforcement, and cholinergic inputs—disinhibit excitatory neurons, leading to ramping responses that integrate over longer timescales (Fu et al., 2015; Pi et al., 2013; Szadai et al., 2022).

The heterogeneous rise and decay dynamics we observe can be explained by a combination of intrinsic, synaptic, circuit, and modulatory mechanisms, with E/I (excitatory/inhibitory) motifs playing a key role in shaping this diversity. At the **intrinsic level**, neurons differ in their ion channel composition, such that strong A-type K^+ currents drive rapid repolarization and narrow responses, while persistent Na^+ or slow Ca^{2+} currents sustain activity and generate broader responses (Hodgkin & Huxley, 1952; Marder & Goaillard, 2006). **Synaptic inputs** also vary in their filtering properties: differences in release probability, vesicle pool size, and receptor kinetics produce characteristic time constants, with some synapses showing rapid depression and others facilitation, and receptor subtypes (e.g., AMPA vs. NMDA, GABA A vs. GABA B) contributing fast or slow components (Abbott & Regehr, 2004; Zucker & Regehr, 2002). Beyond single-cell properties, the **E/I balance in recurrent circuits** amplifies this diversity, as neurons within inhibitory-dominated loops recover quickly, while those in excitatory-rich loops maintain activity longer. Finally, **neuromodulators** further shape kinetics in a cell-type-specific manner:

acetylcholine recruits VIP interneurons to gate inhibition in V1 (Fu et al., 2015; Pi et al., 2013), noradrenaline broadens integration times and enhances ramping dynamics (Sara & Bouret, 2012), and dopamine adjusts recurrent integration in prefrontal networks (Seamans & Yang, 2004).

Limitations of the study

We restricted our analyses to layer 2/3 neurons in V1 and PPC. Other cortical layers, particularly layer 5, may contribute more directly to predictive computations since they integrate top-down and thalamic inputs (Harris & Shepherd, 2015; Maristany de las Casas et al., 2025; Vélez-Fort et al., 2014). Our cell-type coverage was also limited to excitatory, SST, and VIP neurons. Other inhibitory populations such as NDNF interneurons—shown to disinhibit PV cells and gate long-range inputs in layer 1—likely shape predictive signals and could play a role in temporal predictive processing (Abs et al., 2018; Ibrahim et al., 2021).

In addition, we used two-photon calcium imaging, which provides only an indirect proxy of spiking activity. The slow kinetics of calcium indicators blur fast transients, potentially biasing the estimation of timescales and attenuating high-frequency components of neural responses (Wei et al., 2020; Zhang et al., 2023).

We also did not perform intrinsic-signal retinotopic mapping. Although recordings were centered in V1 (**Supp Fig. 1**), the absence of mapping means that some fields of view could overlap with higher visual areas, which may differ in their dynamics and contributions to predictive processing (Garrett et al., 2020; Zhuang et al., 2017).

Finally, while stimulus orientation was varied across tens of trials, the present study focused specifically on temporal structure rather than stimulus identity. Our findings therefore do not address prediction or prediction-error signals related to what stimulus appears, but only those related to when it appears.

Discussion summary

Neural dynamics in V1/PPC during passive audio-visual stimulation are consistent with stimulus-reset relaxation in recurrent networks with diverse timescales, shaped by local inhibitory–excitatory motifs and neuromodulation. Our findings argue against temporal scaling of a single trajectory and instead support distributed tiling of intrinsic trajectories. While omission responses in visual cortex reflect elapsed-time signals, other regions such as hippocampus and cerebellum remain strong candidates for temporal predictive processing. Finally, prior work suggests that active engagement, top-down input, and reward contingencies can recruit prediction and error signals in sensory areas, raising the testable hypothesis that task demands may shift V1 and PPC from intrinsic elapsed-time coding toward explicit temporal predictive processing.

Methods

Subjects

Female and male transgenic mice were used in the current study. Mice included VIP-tdTomato and SST-cre (Jackson 013044) lines. VIP-tdTomato line was produced by breeding VIP-cre (Jackson 031628) with Ai14 (Jackson 007914; cre-dependent tdTomato). All procedures were approved by the Institutional Animal Care and Use Committee at the Georgia Institute of Technology and agreed with guidelines established by the National Institutes of Health.

Number of samples and statistical tests

Ten mice (both male and female) were used: 5 for PPC imaging and 5 for V1 imaging. A total of 18,904 V1 neurons and 14,835 PPC neurons were imaged across all sessions. Approximately 10% did not pass temporal receptive field modeling criteria (see below) and were excluded. Counts of neurons by cell type and area across session types are provided in Table 1.

Each mouse received 5 random sessions, followed by 10–15 fixed/jittered sessions, and then 10–20 short/long sessions. All sessions contained 2,000 audiovisual stimuli. Fixed/jittered sessions included 5 fixed blocks and 5 jittered blocks per session. Approximately 4% of ISIs in fixed/jittered sessions were 'deviant', evenly split between short- and long-deviant ISIs. Short/long sessions included 24 short blocks and 24 long blocks per session.

Comparisons of distribution means were performed using the two-tailed Mann–Whitney U test. Comparisons of variances were performed using the two-tailed Levene's test. Statistical significance was defined as $p < 0.05$.

Region	Cell type	Random	Fixed/jittered	Short/long	Total
V1	**Excitatory**	2,226	5,634	7,101	**14,961**
	VIP	597	692	1,233	**2522**
	SST	181	600	640	**1421**
	Total	**3,004**	**6,926**	**8,974**	**18,904**
PPC	**Excitatory**	2,437	5,327	3,913	**11,677**
	VIP	304	678	401	**1,383**
	SST	319	839	617	**1,775**
	Total	**3,060**	**6,844**	**4,931**	**14,835**

Table 1. Number of imaged neurons per brain region, cell type, and paradigm.

Behavioral paradigms and stimulus design

Auditory and visual stimuli were always presented simultaneously and lasted 200 ms on each repetition. The ISI was defined as the absence of tone accompanied by a gray screen. The auditory stimulus was an 11 kHz pure tone, and the visual stimuli were gratings of four orientations (0°, 45°, 90°, 135°). The same grating orientation was presented for randomly 15-20 consecutive trials before switching to another randomly-selected orientation. Orientation changes did not occur for 3 trials immediately after transitioning to a new block (in both fixed/jittered and short/long sessions) or for 3 trials at the end of each block. Grating orientation changes were not analyzed in this study.

Experiments involved 3 paradigms (session types): random, fixed/jittered, and short/long sessions. In random sessions, ISIs were drawn from a uniform distribution (0.5–2.5 s). In fixed/jittered sessions, blocks of 200 trials alternated between fixed ISIs (1.5 s) and jittered ISIs (uniform distribution: 0.5–2.5 s). 4% deviant ISIs were included, split between short (0.5 s), or long (2.5 s) ISIs. In short/long sessions, blocks of 50 trials alternated between short ISIs (1 s) and long ISIs (2 s).

Visual stimuli were displayed on a monitor (Dell, G2524H) covered with a blue screen filter (Amazon) to minimize imaging artifacts during stimulus presentation.

Surgical procedure: window craniotomy

Stereotaxic surgeries (David Kopf, Instruments; Models 942 and 1900) were performed under isoflurane inhalation anesthesia (Somno; Kent Scientific). Anti-inflammatory drug Dexamethasone (1-2mg/kg) was subcutaneously injected 24h and 1h before the surgeries. Post-op care involved subcutaneous injection of the analgesic drug Ketoprofen (2-5 mg/kg). During the surgery, 0.1-0.2mL sterile saline was Intraperitoneally (IP) injected to compensate for liquid loss.

A circular craniotomy in 3mm diameter using a biopsy punch (Fischer Scientific) was made over the left PPC (Najafi et al.) (stereotaxic coordinates: 2mm posterior to bregma, 1.7mm lateral) or the left V1 (Georgia Bastos et al.) (stereotaxic coordinates: 2.92mm posterior to bregma, 2.0mm lateral).

Injection pipettes (15-20 um in diameter; Drummond Micropipettes 3.5") were back-filled with mineral oil (Sigma Aldrich) and then front-filled with viral vectors: AAV9-Syn-jGCaMP8f (Addgene #162376) for VIP-tdTomato mice, and AAV1-CAG-flex-jGCaMP8f (Addgene #162382) for SST-cre mice. Virus titers was 2.3 x 10^13 gc/mL, and they were both 2-10X diluted in sterile

saline. Virus injections were made (Nanoject III; Thomas Scientific) with the speed 10nl/sec in 3-4 different locations (within 1mm around the coordinate center), each with 500nl virus, and ~150 um below the dura.

A glass plug—made by stacking a 3mm coverslip and a 5 mm coverslip with optical bond (Norland Optical Adhesive NOA 81; Edmund Optics)—was used to cover the craniotomy window. Vetbond (Amazon) and metabond (C&B Metabond® Quick Adhesive Cement System; Parkell Inc.) were used to seal the craniotomy window. Black cement (Ortho-Jet BCA) was applied to reduce possible light leakage during optical imaging.

Two-photon calcium imaging

Two-photon calcium imaging data were acquired using a Bruker Ultima 2Pplus laser-scanning microscope (Nikon objective: 16X; NA 0.8; Chroma emission filters: 520/40-2p for the green channel and 660/40-2p for the red channel). All imaging experiments were conducted in darkness. The microscope objective was immersed in water-based ultrasonic gel, and the objective was covered with black electrical tape to minimize light leakage. After surgical recovery, mice were habituated to the setup for 1–2 days before imaging sessions commenced. Each session lasted ~1 hour. During each session, calcium imaging videos (512 × 512 pixels, 30 Hz), stimulus voltage traces (10 kHz), and high-speed videos of the mouse's left eye were recorded (30 Hz; FLIR camera; Lens: CM3-U3-13Y3M-CS 16mm; each video frame triggered by the imaging scope).

Preprocessing imaging data

We used a customized pipeline based on suite2p (Pachitariu et al., 2017) to extract neurons and their activity from the imaging videos. Raw videos were imported into suite2p to identify regions of interest (ROIs) and their raw fluorescence traces. As an initial quality control step, ROIs with a compactness value greater than 1.06 were excluded to remove poorly segmented ROIs with abnormal geometry. For each trace, a Gaussian filter ($\sigma = 600s$) was applied to estimate the fluorescence baseline and compute ΔF/F as $\frac{(F_{fluo}-F_{base})}{F_{base}}$, where F_{fluo} is the raw fluorescence signal and F_{base} is the extracted baseline from the Gaussian filter. Finally, each neuron's ΔF/F trace was z-scored individually.

Identification of VIP interneurons

We used the 'cellpose' algorithm (Stringer & Pachitariu, 2025) to identify VIP interneurons labeled with tdTomato in the red channel. For each segmented ROI, we collected the corresponding functional mask from the green channel and quantified red–green co-localization with an overlap score based on intersection-over-union as $s = \frac{|R \cap G|}{|R \cup G|}$, where R and G are the tdTomato and GCaMP masks, respectively. Neurons were then classified as excitatory ($s \leq 0.3$), uncertain ($0.3 < s < 0.7$), or VIP ($s \geq 0.7$). Here, the two thresholds (0.3, 0.7) were chosen a priori based on empirical validation.

Temporal receptive field (TRF) model

We modeled single-neuron temporal responses around a stimulus using an ex-Gaussian temporal receptive field (TRF) model (**Fig. 1I; Fig. 6C,E; Supp Fig. 3**). The model has been successfully used to analyze the neural ramping dynamics in the anterior lateral motor cortex (Affan et al., 2024), medial prefrontal cortex (Cao et al., 2024), and entorhinal cortex (Bright et al., 2020). A similar model also has been used to reveal sequential firing in hippocampus and prefrontal cortex (Cruzado et al. 2020).

This model, denoted as $TRF(t) = (G * E)(t)$, is defined as

$$TRF(t; b, a, m, r, \tau) = b + \frac{a}{2} \exp\left(\frac{2m + r^2}{2\tau} - \frac{t}{\tau}\right) erfc\left(\frac{m + \frac{r^2}{\tau} - t}{\sqrt{2}r}\right),$$

where $erfc$ denotes the error function. This form results from convolving a Gaussian kernel G:

$$G(t; m, r) = \frac{1}{\sqrt{2\pi}r} \exp\left(-\frac{(t-m)^2}{2r^2}\right),$$

with a causal exponential decay E:

$$E(t; \tau) = \frac{1}{\tau} \exp\left(-\frac{t}{\tau}\right).$$

Here, $b \in \mathbb{R}$ is the baseline offset, $a > 0$ represents the absolute response amplitude, and $m \in \mathbb{R}$ denotes the response latency (mean of the Gaussian kernel). The parameter $r \in (0,1)$ controls temporal receptive field width, with smaller values yielding narrower Gaussian kernels. The exponential component is governed by $\tau > 0$, which sets the timescale of ramp-up or ramp-down. Responses with larger τ decay more slowly back to baseline. For interpretability, we use $\frac{1}{\tau}$ to represent ramping speed.

To fit the TRF model to a neuron (**Fig. 1l**), we aligned the neural activity during the interval before and the one after stimulus onset at $t = 0$. Time was normalized for fitting stability, denoted as $t_- \in [-1,0]^{n_1}$ and $t_+ \in [0,1]^{n_2}$, respectively, where n_1 and n_2 are the number of time points.

Let $x_- \in [0,1]^{n_1}$and $x_+ \in [0,1]^{n_2}$ be the two segmentations of the normalized activity, referring to the pre-stimulus and post-stimulus activity, respectively. We then fit $TRF(-t; b, a, m, r, \tau)$ to x_- and fit $TRF(t; b, a, m, r, \tau)$ to x_+ , which we refer to as ramp-up and ramp-down models, respectively (**Fig. 1l**). Note that both models have the same parameters, but they are fit to inputs of opposite direction (flipped in time). The ramp-up and ramp-down models differ only by the direction of the time input (forward vs reversed). This gives two sets of parameters $\theta_- = \{b_-, a_-, n_-, r_-, \tau_-\}$ and $\theta_+ = \{b_+, a_+, n_+, r_+, \tau_+\}$, referring to the *ramp-up* and the *ramp-down* model components. Note that this model always assumes that each neuron has both the ramp-up component, before stimulus, and ramp-down component, after stimulus. The goodness of fit is evaluated by the coefficient of determination between the prediction and the ground-truth normalized activity for both components.

Clustering neural responses

We used a combination of generalized linear modeling (GLM) (Garrett, Groblewski, Piet, Ollerenshaw, Najafi, et al., 2023; Steinmetz et al., 2019) and the TRF model prior to clustering (**Fig. 1l**). For each paradigm, neural responses from all sessions were pooled together, and the following steps were performed on the combined dataset.

1) GLM modeling. High-sampling-rate voltage recordings of the stimulus trace (10 kHz) were first aligned with the fluorescence traces, for the entire 1hr session, using nearest-neighbor interpolation. For each neuron, we fit a GLM to the z-scored ΔF/F trace $f \in \mathbb{R}^{N_{time}}$ using the binary stimulus trace $S \in \{0,1\}^{N_{time}}$ as input, over the window $[-1500,1500]$ ms relative to stimulus onset (N_{time} denotes the number of imaging frames in a session, with 1 indicating stimulus presentation and 0 indicating no stimulus). This window was determined such that we can fit the TRF model easily for the incoming steps. To prevent overfitting and obtain smooth kernel estimates, we applied L2 regularization $\alpha = 5 \times 10^4$multiplier). The GLM kernel for the i-th neuron $k_i \in \mathbb{R}^{n_k}$ was then estimated via the least square principle $k_i = (S^T S)^{-1} S^T f$.

Next, since the fit convolution kernel is flipped from the actual GLM kernel, we flipped the resulting GLM kernel to correct this. We then split the fit GLM kernel k_i into two parts, $k_{i-}(t)$

with $t < 0$ and $k_{i+}(t)$ with $t > 0$, which are therefore the summaries of how a neuron generally responds before and after a stimulus, respectively.

2) TRF modeling. See the Methods section 'Temporal receptive field (TRF) model' for details. In brief, for each neuron, we fit 2 TRF models to the 2 components of the GLM kernel, $k_{i-}(t)$ *and* $k_{i+}(t)$, corresponding to the ramp-up and ramp-down models, respectively:

$\theta_{(i)-} = \{b_{(i)-},\ a_{(i)-},\ n_{(i)-},\ r_{(i)-},\ \tau_{(i)-}\}_{i=1}^{N_{neuron}}$, and

$\theta_{(i)+} = \{b_{(i)+},\ a_{(i)+},\ n_{(i)+},\ r_{(i)+},\ \tau_{(i)+}\}_{i=1}^{N_{neuron}}$.

Let $R^2_{(i)-}$ and $R^2_{(i)+}$ denote the goodness of fit for the two models. We defined ramp-up neurons as the neurons that can fit (1) well with the ramp-up model, and (2) better than the ramp-down model, and vice versa. Let θ be the threshold ($\theta = 0.3$ in this paper).

Thus, those neurons with both $R^2_{(i)-} > \theta$ and $R^2_{(i)-} > R^2_{(i)+}$ are determined as the ramp-up neuron, while those neurons with both $R^2_{(i)+} > \theta$ and $R^2_{(i)+} > R^2_{(i)-}$are the ramp-down neuron. All other neurons with both goodness of fit lower than the threshold is not included in further analysis (~10%). Therefore, this thresholding serves the quality control procedure in this paper, resulting in N_{up} ramp-up neurons and N_{down} ramp-down neurons.

3) K-means clustering. After getting the two board categories of neurons, within each ramp-up and ramp-down group, we use k-means on the fit parameter $\{r_{(i)-}\}_{i=1}^{N_{up}}$ and $\{r_{(i)+}\}_{i=1}^{N_{down}}$ to find subgroup of neurons with distinct temporal receptive fields. The number of clusters is determined such that the Silhouette Coefficient is maximized.

Time scaling analysis

To test for potential temporal scaling effects (Fig. 3), we performed the following procedures. Let $t_{src} \in \mathbb{R}^{n_{src}}$ denote the original time stamps for an aligned neural trace and $t_{des} \in \mathbb{R}^{n_{des}}$ denote the target time range to which the trace was scaled, where n_{src} and n_{des} are the respective length of the time stamps. Scaled time stamps were computed as:

$t_{scaled} = \frac{t_{src}}{n_{src}} \times n_{des}$.

A nearest neighbor interpolation was then used to map t_{scaled} to t_{des}. This procedure left the neural activity values unchanged but adjusted the time axis to match the target interval. Given

neural activity aligned to stimulus onset, we applied this scaling separately to the pre-stimulus and post-stimulus intervals, while leaving the activity during the stimulus itself unchanged.

Modulation index for deviant ISIs in fixed/jittered sessions

We quantified condition-evoked changes (**Supp Fig. 2**) with a symmetric modulation index defined as

$$m = \frac{v_{post} - v_{pre}}{|v_{post}| + |v_{pre}|} ,$$

where v_{pre} and v_{post} are the average signal within the pre- and post-event windows. This normalization bounds the index in $[-1,1]$, is invariant to overall scaling, and treats increases and decreases symmetrically ($m > 0$: relative increase after the event; $m < 0$: decrease; and $m = 0$ no change).

- Positive prediction error (stimulus after deviant ISI; Fig. 4, red dashed line; both short/long blocks): Responses were averaged over [0,300] ms relative to stimulus onset. v_{pre} was aligned to the pre-deviant stimulus, v_{post} to the post-deviant stimulus (Supp. Fig. x); hence, the modulation index reflects response modulation relative to the 'standard' stimulus.
- Negative prediction error (unexpected omission during long deviant ISIs; Fig. 4, yellow dashed line): $v_{pre}$was taken from the 300 ms preceding the expected stimulus, and v_{post} from the time of the expected stimulus onset; hence, the modulation index reflects response modulation relative to baseline immediately before the omission.

Population trajectory analysis

Given aligned neural activity, we first averaged responses across trials, yielding a data matrix: $x \in \mathbb{R}^{n_{neuron} \times n_{time}}$. Principal component analysis (PCA) was applied to extract latent population dynamics, with the first three PCs (highest explained variance) used for visualization. To obtain smoother neural trajectories, each PC was interpolated to increase the number of time points fourfold, followed by Savitzky–Golay filtering (polynomial order = 3, window size = 8).

Temporal decoding analysis

To evaluate how neural populations encode elapsed time (Fig. 6), we trained classifiers to discriminate neural activity between pairs of time bins within an interval. Neural data were aligned to stimulus onset and truncated at the onset of the next stimulus. Each time bin was defined as two non-overlapping imaging frames, with neural activity averaged within each bin for every neuron and trial.

To reduce single-trial noise in calcium imaging, we used a bootstrapping approach: on each iteration (n=250), pseudo-trials were generated by averaging random subsets of three trials.

To control for population-size differences across clusters, neurons were randomly subsampled (n=25) to a fixed number (n = 120) in each bootstrap iteration. The resulting data tensor was denoted as:

$x \in \mathbb{R}^{n_{trials} \times n_{neurons} \times n_{time}}$, where n_{trials}, $n_{neurons}$, n_{times} are the number of pseudo trials, neurons, and time bins, respectively.

For each pair of time bins, pseudo-trials were split into training and test sets (80/20 split). A Support Vector Machine (SVM) classifier with a linear kernel was trained on data shaped as $n_{neurons} \times (n_{trials} \times n_{time})$. This train/test procedure was repeated 25 times using stratified randomized folds, which ensured that both time bins were equally represented in each split. The decoding accuracies from a total of $N_{trial\ bootstrp} \times N_{neuron\ subsample} \times N_{splits}$ repetitions (250 trial bootstraps, 25 neuron subsamples, and 25 splits) were averaged to provide a stable estimate. This procedure was repeated across all time-bin pairs, and the results were assembled into a time-by-time accuracy matrix: $ACC \in [0,1]^{n_{time} \times n_{time}}$.

Data and code availability

All data used in this paper will be made public upon the paper publication. Code for data processing and analysis is publicly available on Najafi Lab GitHub page: https://github.com/najafi-laboratory/2p_imaging/tree/main/passive_interval_oddball_202412

Acknowledgments

We are grateful to the Haider Lab for providing the SST-Cre mice, to Simone Russo for thoughtful discussions, to Laurence Copeland and Vanshika Mehta for assistance with early experiments, and to Joey Broussard, Robert Howard, and Leslie Claar for technical expertise. This work was supported by awards to F.N. from the Whitehall Foundation, the Research

Corporation for Science Advancement (Scialog), and the Chan Zuckerberg Initiative (CZI).

Author contributions

Y.H.: Experiments; Data analysis; Conceptualization; Writing

A.S.: Clustering method (initial version); Help with figure preparation

M.C., S.W.: Help with imaging experiments

T.S.: Engineering support

S.M.: Histology

F.N.: Conceptualization; Writing; Supervision; Funding acquisition; Resources

Declaration of interests

The authors declare no competing interests.

Figure 1

A Scientific Question:
temporal predictive processing vs. temporal signaling

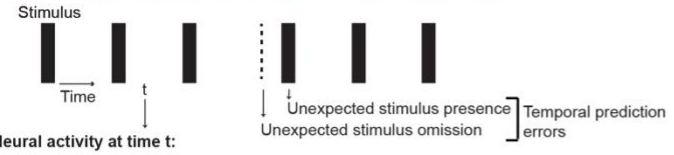

Neural activity at time t:

1) Elapsed time since the previous stimulus → **temporal signaling**
2) Predicted timing of the next stimulus (temporal predictions) and timing violations (temporal prediction errors) → **temporal predictive processing**

B Two-photon calcium imaging during passive audio-visual stimulation in awake mice

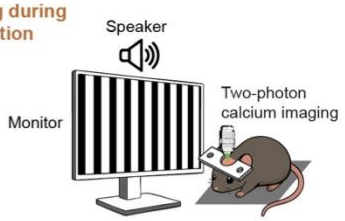

C Example imaging field-of-view from visual cortex

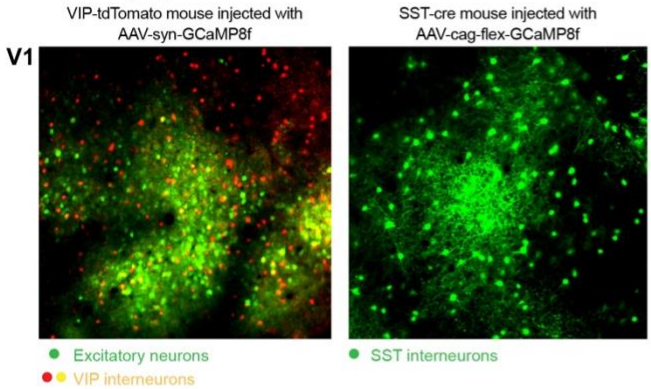

D Example imaging field-of-view from parietal cortex

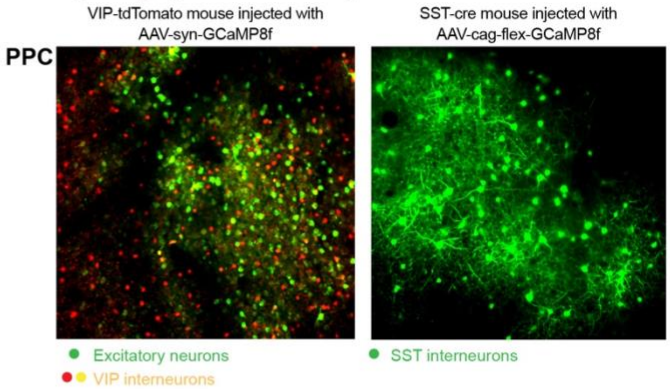

E Example calcium traces

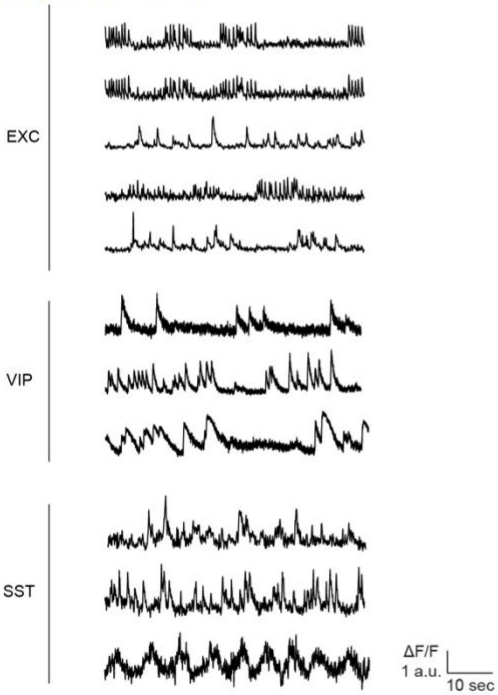

Three behavioral paradigms (session types)

F Short/long-interval sessions

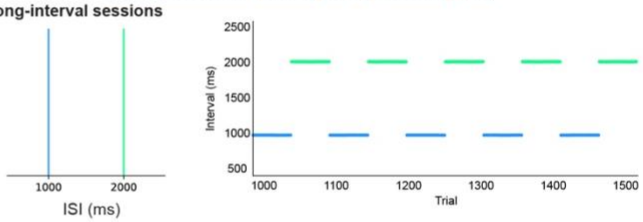

G Fixed/jittered-interval sessions

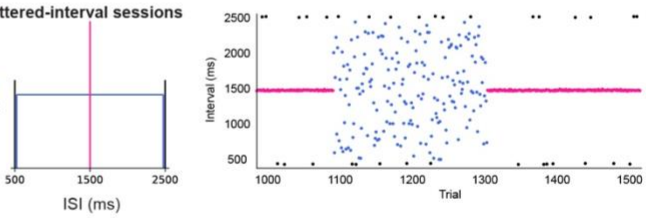

H Random-interval sessions

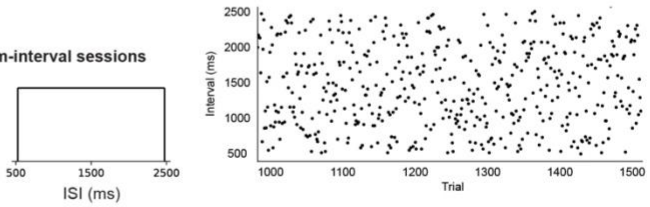

I Clustering methodology

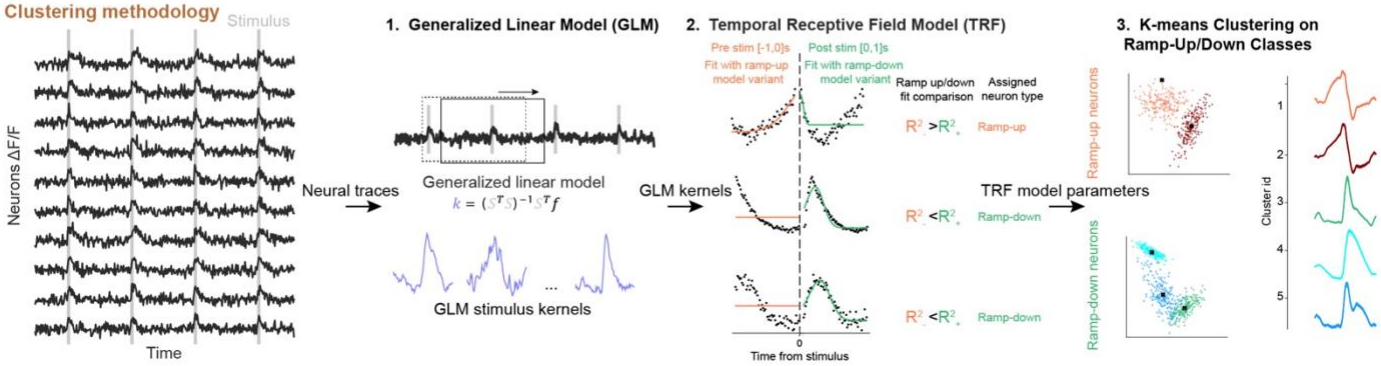

Figure 1. Experimental design to disentangle temporal signaling from temporal predictive processing.

A) Neural activity at each timepoint could reflect one of the 2 processes: (1) temporal signaling, i.e., encoding elapsed time since the previous stimulus; or (2) Temporal predictive processing, i.e., generating predictions and prediction errors about the timing of the upcoming stimulus. Temporal prediction errors occur when a stimulus is presented earlier or later ('omission') than expected.

B) Awake, head-fixed mice received repeating audio-visual stimuli (0.2s), separated by an inter-stimulus interval (ISI), while two-photon calcium imaging was performed from the visual cortex and posterior parietal cortex (PPC).

C) Visual cortex imaging field of view. Two example sessions. **Left:** VIP-tdTomato mouse injected with GCaMP8f. All neurons express GCaMP8f; a subset is in red, labeling VIP interneurons. Red and yellow: VIP interneurons. Green: presumptive excitatory neurons. **Right:** SST-cre mouse injected with cre-dependent GCaMP8f. Green: SST interneurons.

D) Same as C, but for PPC.

E) Example fluorescence traces for excitatory, VIP, and SST neurons.

F–H) Mice received three paradigms (session types) distinguished by their ISIs. **Left:** distribution of ISIs in a session. **Right:** ISIs for example consecutive trials in a session.
F) Short/long sessions had alternating blocks of trials with short (1s; blue) and long (2s; green) ISIs.
G) Fixed/jittered sessions had alternating blocks of trials with fixed (1.5s; pink) and jittered (0.5–2.5s; blue) ISIs. Each block also included 5% deviant ISIs (0.5s and 2.5s, black).
H) In random sessions all trial ISIs were random (0.5–2.5s).

I) Clustering methodology. **1)** <u>GLM model:</u> neural responses across the full session were modeled with a GLM using stimuli as input. **2)** <u>TRF model:</u> two temporal receptive field model variants, with opposite input polarity, were applied to the pre- and post-stimulus components of each kernel to get the ramp-up and ramp-down model responses, respectively. Goodness-of-fit comparisons determined whether each neuron was classified as ramp-up or ramp-down. **3)** <u>K-means clustering:</u> finally, neurons within each class were clustered using K-means on the model parameters.

Figure 2

Neurons classify as stimulus-inhibited (ramp-up) or stimulus-activated (ramp-down) with additional subtypes.

Cell type contributions vary across clusters.

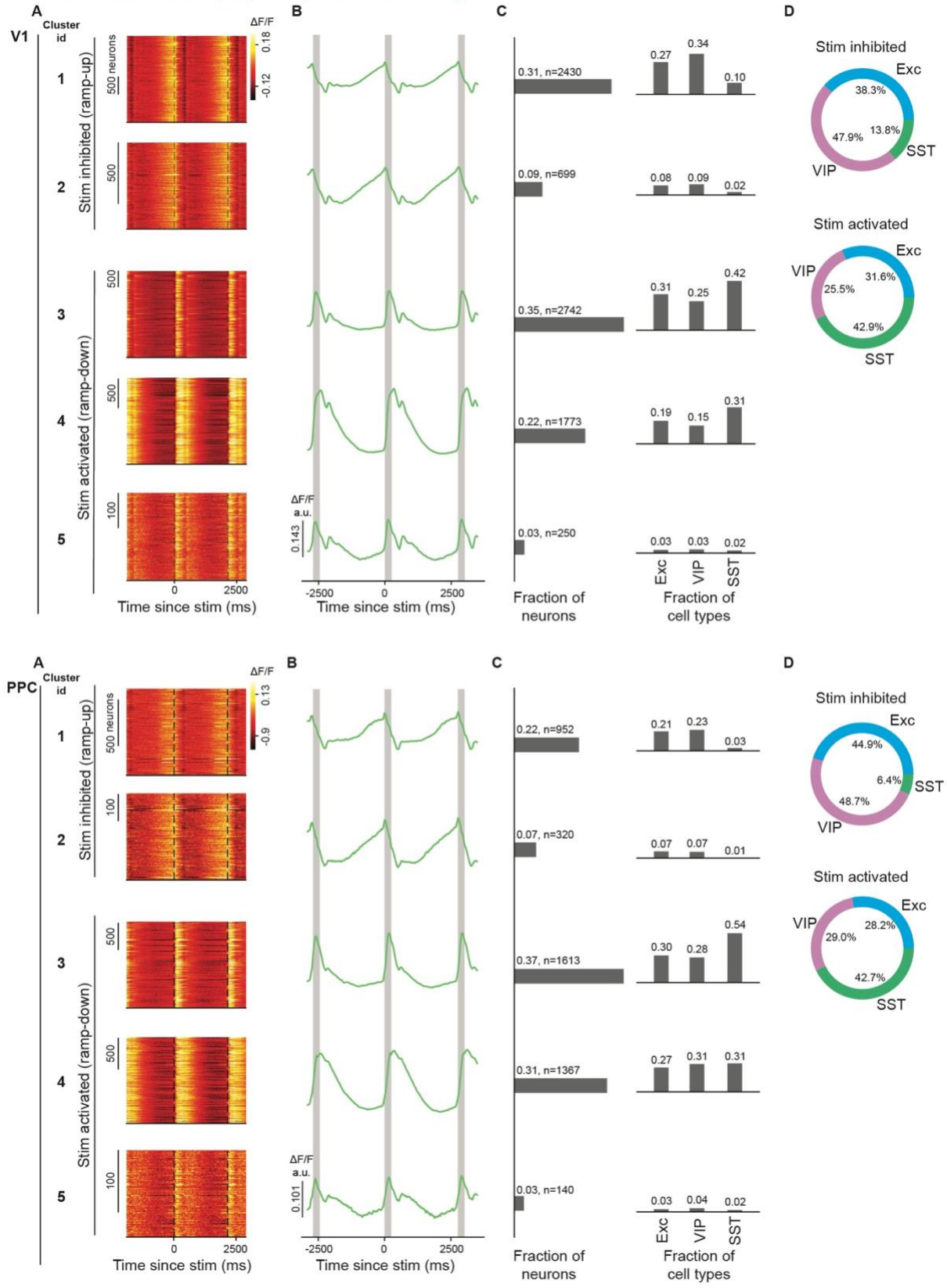

Figure 2. V1 and PPC neurons demonstrate stimulus-evoked and ramping dynamics to repeating audio-visual stimuli.

Data from the long block of short/long sessions. Clusters were identified on pooled neurons across all short/long sessions. **Top panels:** V1; **Bottom panels:** PPC.

A) Heatmaps show trial-averaged, single-neuron activity (ΔF/F) for each cluster (top to bottom). The stimulus-inhibited (ramp-up) and stimulus-activated (ramp-down) labels on the left are based on the temporal receptive field model, and the subtypes within each group (heatmap) are identified by k-means clustering.

B) ΔF/F, mean ± SEM across neurons and trials, for each cluster (top to bottom). Gray boxes: stimuli.

C) Left: fraction of all neurons assigned to each cluster. **Right:** fraction of neurons of each cell type assigned to each cluster. Clusters were identified on pooled neurons across all short/long sessions.

D) Fraction of cell types within each broad class of stimulus-inhibited (top), and stimulus-activated (bottom).

Figure 3

Larger stimulus-evoked and ramping responses occur in long-interval blocks.

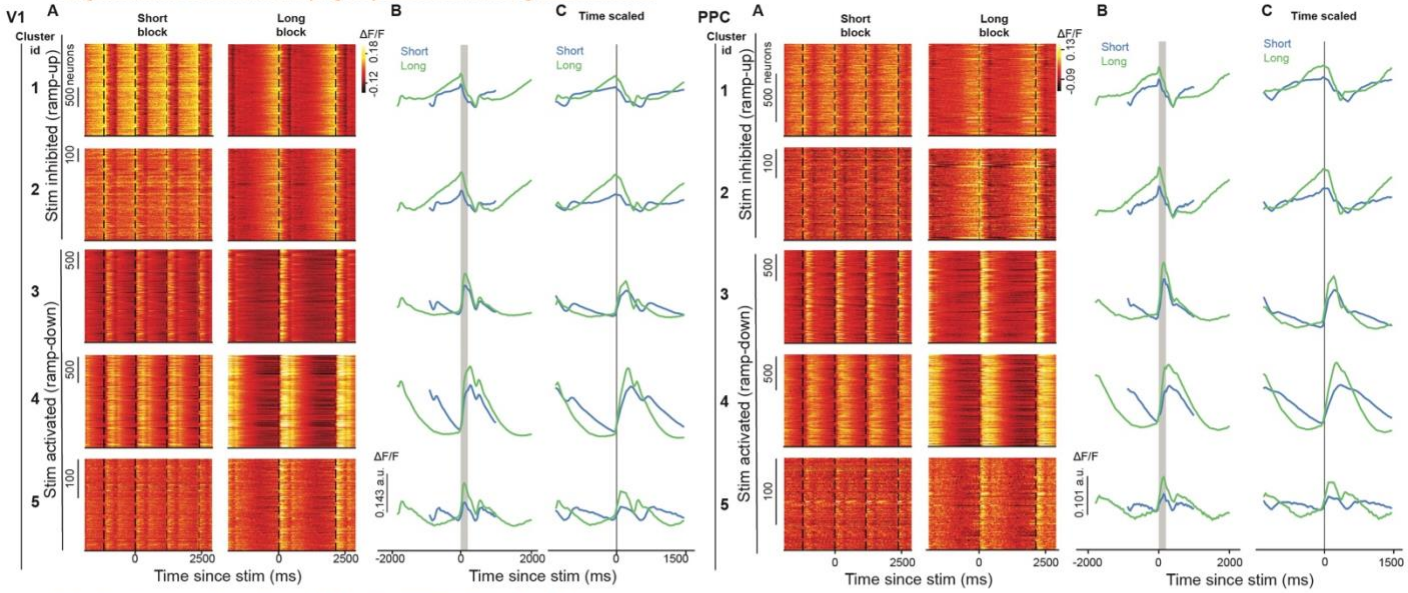

Neural responses change immediately with short/long block switches.

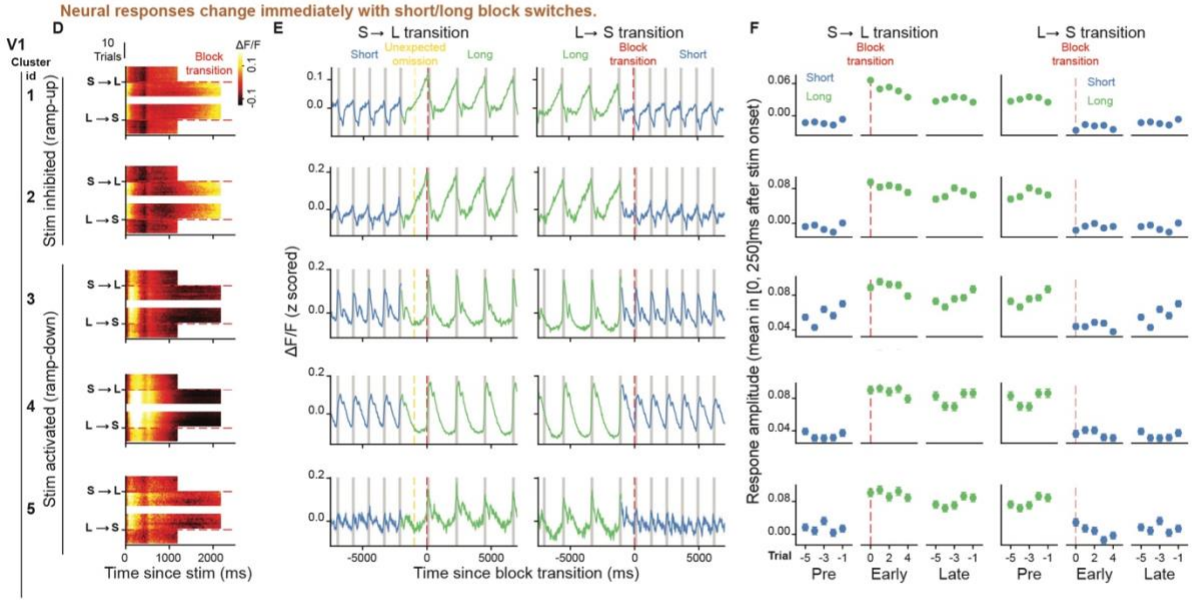

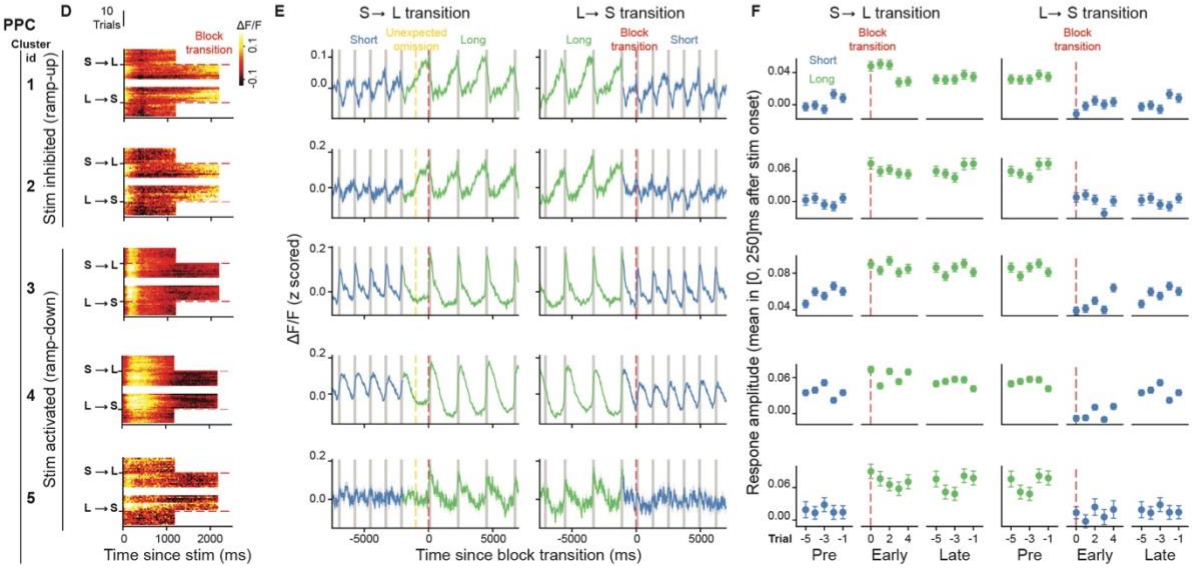

Figure 3. Interval transitions evoke immediate, non-gradual neural response changes.

Data from the short/long sessions, comparing short- and long-block responses (**A-C; left panels:** V1; **right panels:** PPC**)**, and demonstrating rapid response changes with block transitions (**D-F; top panels:** V1; **bottom panels:** PPC. Clusters are the same as in Fig. 2. Each row corresponds to a cluster.

A) Heatmaps of trial-averaged, single-neuron activity aligned on stimuli (vertical lines) in the short (**Left**) and long (**Right**) blocks, for each cluster (top to bottom). Neurons are sorted identically on the left and ride sides.

B) Neuron- and trial-averaged activity superimposed for short (blue) and long (green) blocks, aligned on the stimulus (gray box).

C) Same as B, but with time scaling to place short and long on the same timescale.

D) Heatmaps of trial-by-trial, population-averaged activity around block transitions (red horizontal lines), for both short-to-long (S→L) and long-to-short (L→S) block switches, for distinct clusters (top to bottom).

E) Trial-by-trial neural activity around block transitions. Same as **C**, but shown as line plots (mean ± SEM across neurons and blocks). Red line: first stimulus after ISI switch for both transitions. Yellow line: expected stimulus timing based on the short block (first unexpected stimulus omission). Blue: short block; Green: long block. Gray boxes: stimuli.

F) Response magnitude quantified in the 300ms window after stimulus onset, for 5 trials before transition (pre), 5 trials immediately after (early), and the last 5 trials of the block (late).

Figure 4

Responses to unexpected stimulus omission or delivery are identical across fixed and jittered temporal contexts.

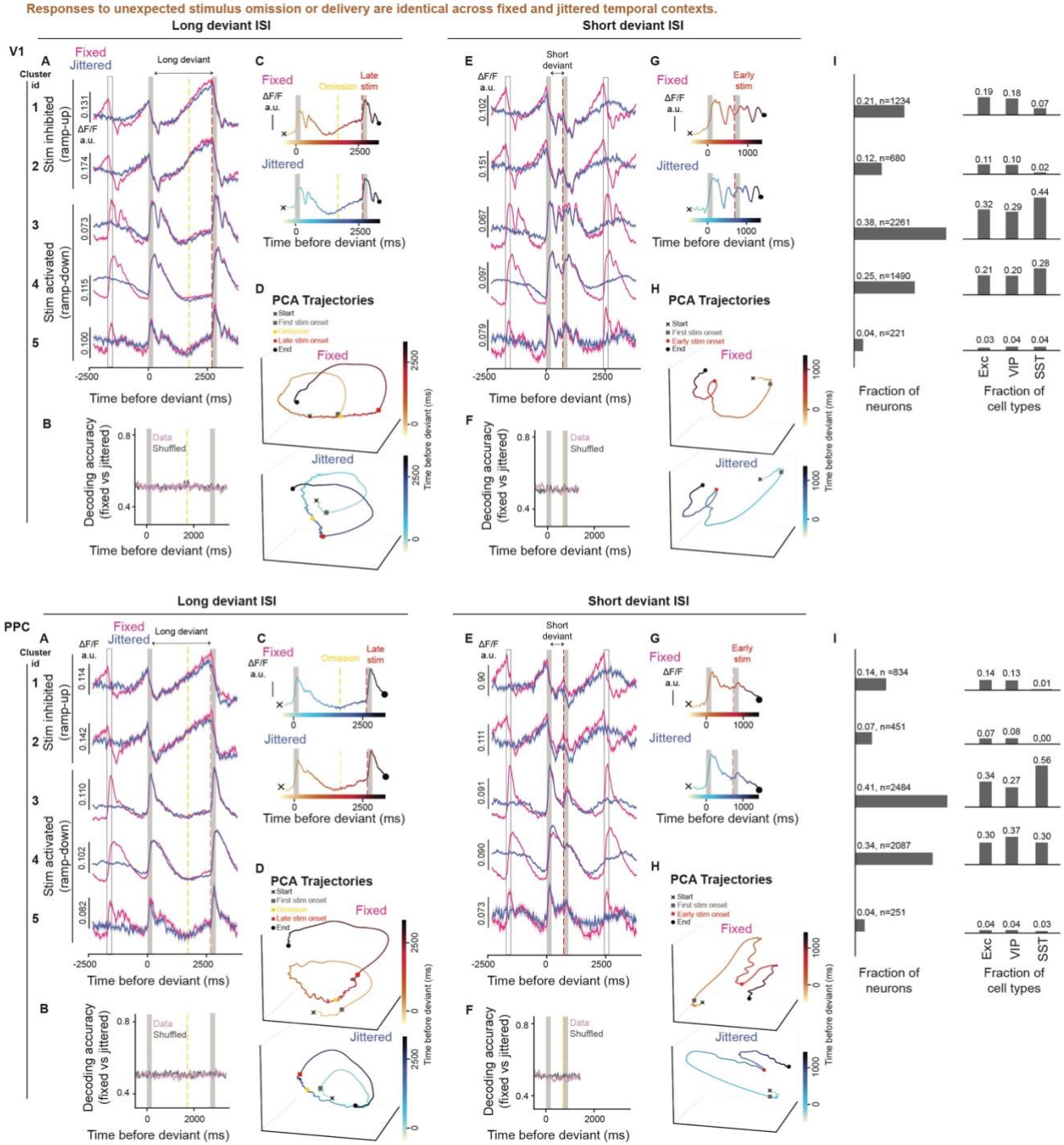

Figure 4. Neural responses do not differ between fixed and jittered blocks for either long or short deviant ISIs.

Data from fixed/jittered sessions, showing identical responses to both short and long deviant ISIs across fixed and jittered blocks. Clusters were identified on pooled neurons across all fixed/jittered sessions. **Top panels:** V1; **Bottom panels:** PPC.

A) Neural responses (mean ± SEM) for each cluster, for fixed (pink) and jittered (blue) blocks, aligned on the stimulus before long deviant ISI (yellow line: expected but omitted stimulus; Gray boxes: stimuli; Empty boxes: stimuli in fixed, and mean stimuli time in jittered).

B) Decoding accuracy for classifying fixed vs. jittered trials (cross-validated; Purple: real data; Gray: shuffled data; Yellow line: omission).

C) Population average (all neurons of all clusters) for fixed (top) and jittered (bottom) blocks, aligned on the long deviant ISI. Traces are color coded to match PCA trajectories in D.

D) PCA population trajectories for fixed (top) and jittered (bottom) trials, aligned on the long deviant ISI. Top 3 PCs shown; Yellow: unexpected omission, due to the long ISI; Red: unexpected late stimulus (stimulus after the long deviant ISI).

E–H) Same as A–D, but aligned on the stimulus after short deviant ISI. Red: unexpected early stimulus (stimulus after the short deviant ISI).

I) Left: fraction of all neurons assigned to each cluster. **Right:** fraction of neurons of each cell type assigned to each cluster.

Figure 5

Ramp-up and ramp-down clusters are present in naive mice, during initial exposure to random stimuli.

Population activity follows a common trajectory across intervals and is reset by each stimulus (F,H).

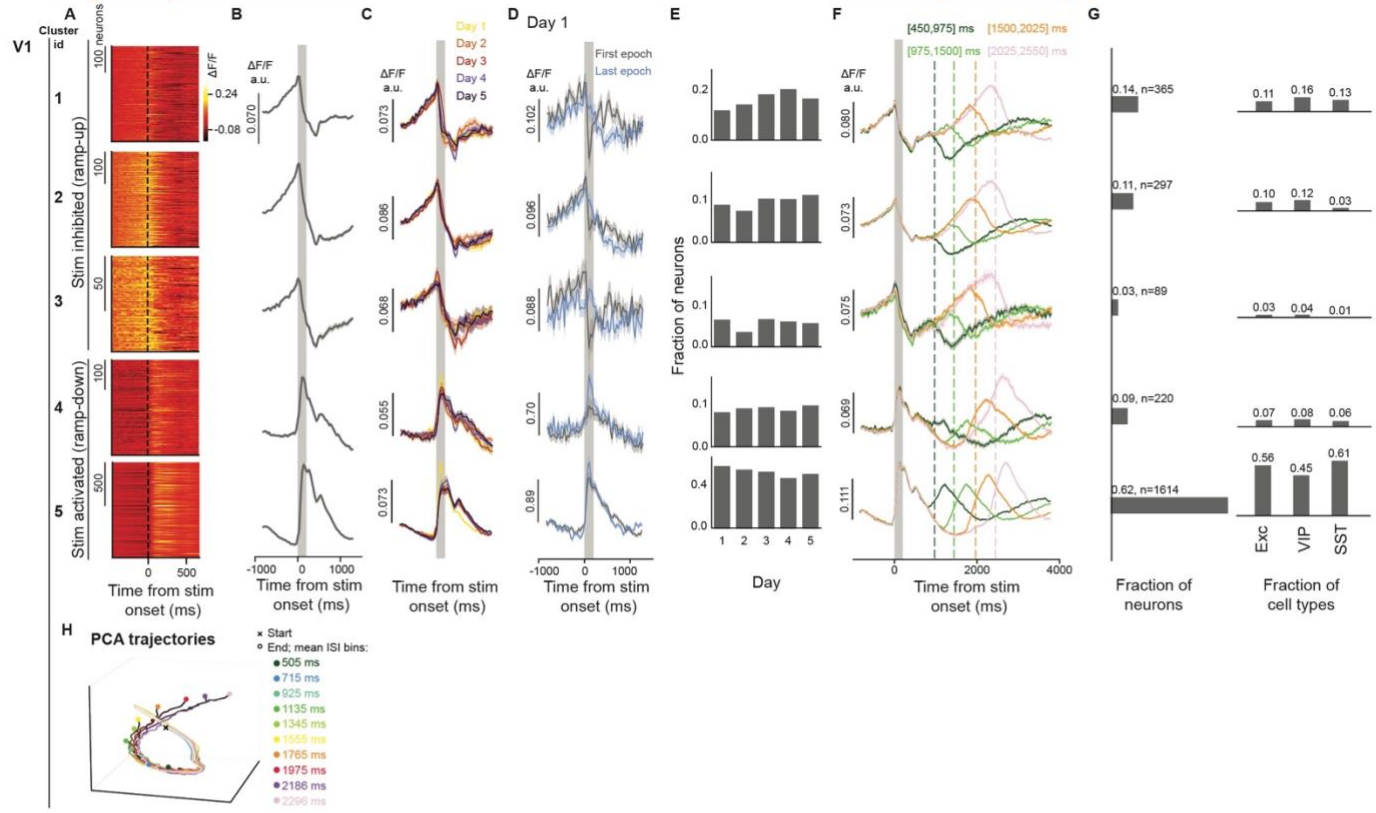

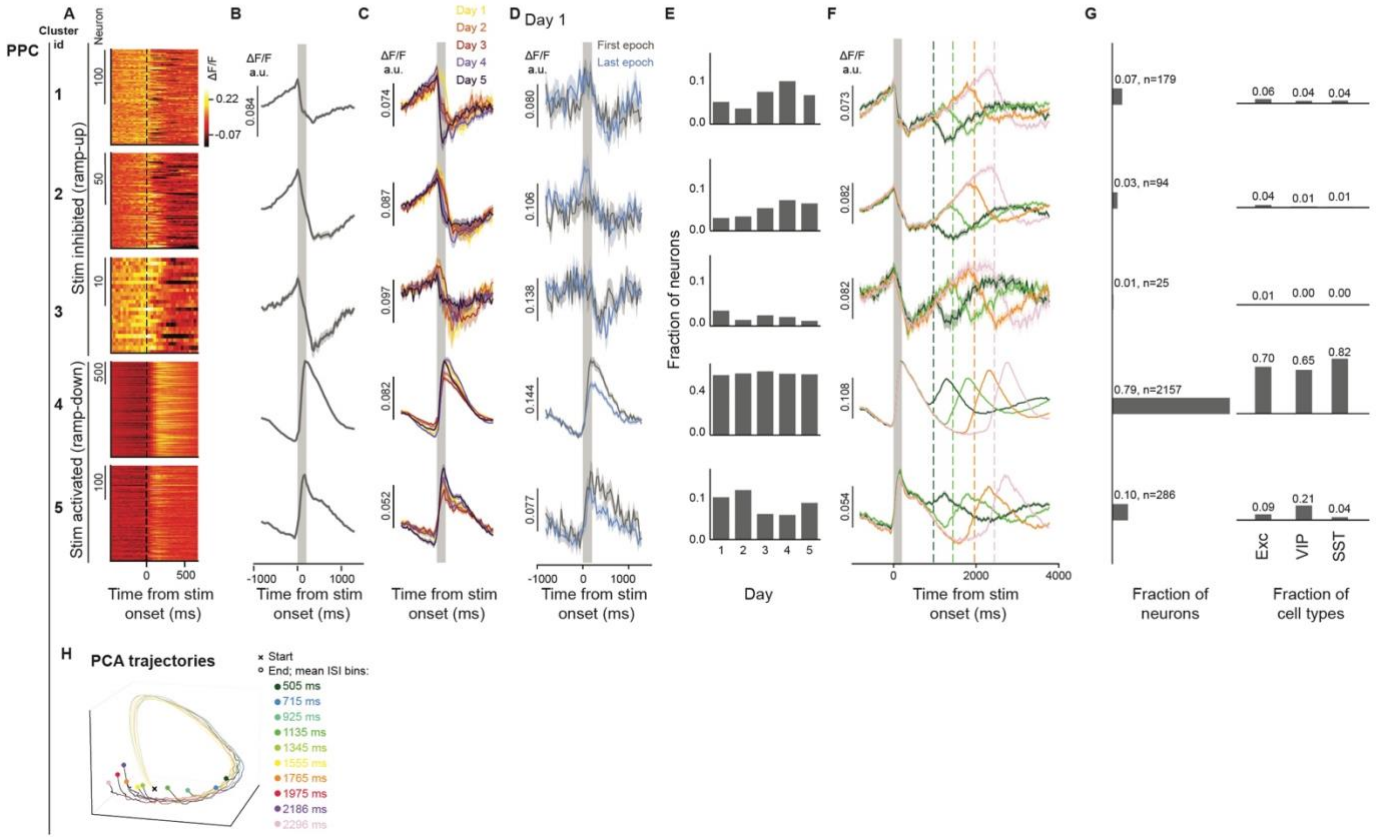

Figure 5. Neural responses during repeating stimuli are intrinsic and not learned.

Data from random sessions, showing that all neural clusters are present from the beginning in naïve mice, and do not require learning to emerge. Clustering was performed on pooled neurons across all random sessions. Each row corresponds to a cluster. **Top panels:** V1; **Bottom panels:** PPC.

A) Heatmaps of trial-averaged, single-neuron activity aligned on stimulus onset (black line), for each cluster (top to bottom).

B) Neuron- and trial-averaged responses aligned on the stimulus (gray box) for each cluster.

C) Averaged responses aligned on the stimulus, same as **B**, but shown separately for individual random sessions (different colors).

D) Averaged responses for the first (gray) and last (blue) 50 trials of the first session.

E) Fraction of total neurons in each cluster distributed across the five random days.

F) Random ISIs divided into four bins (different colors). Neural responses averaged across trials within each ISI bin. Gray box: stimulus. Vertical lines: mean ISI of each bin.

G) Left: fraction of all neurons assigned to each cluster. **Right:** fraction of neurons of each cell type assigned to each cluster.

H) PCA of population activity (top 3 components) from stimulus onset through the ISI. Random ISIs were divided into 10 bins (210 ms each), and trajectories are shown up to the mean ISI for each bin. Trajectories follow a common path across intervals and extend further along it with longer ISIs.

Figure 6

Distinct decoding profiles (B,D) arise from cluster-specific differences in ramping speed and width (E).

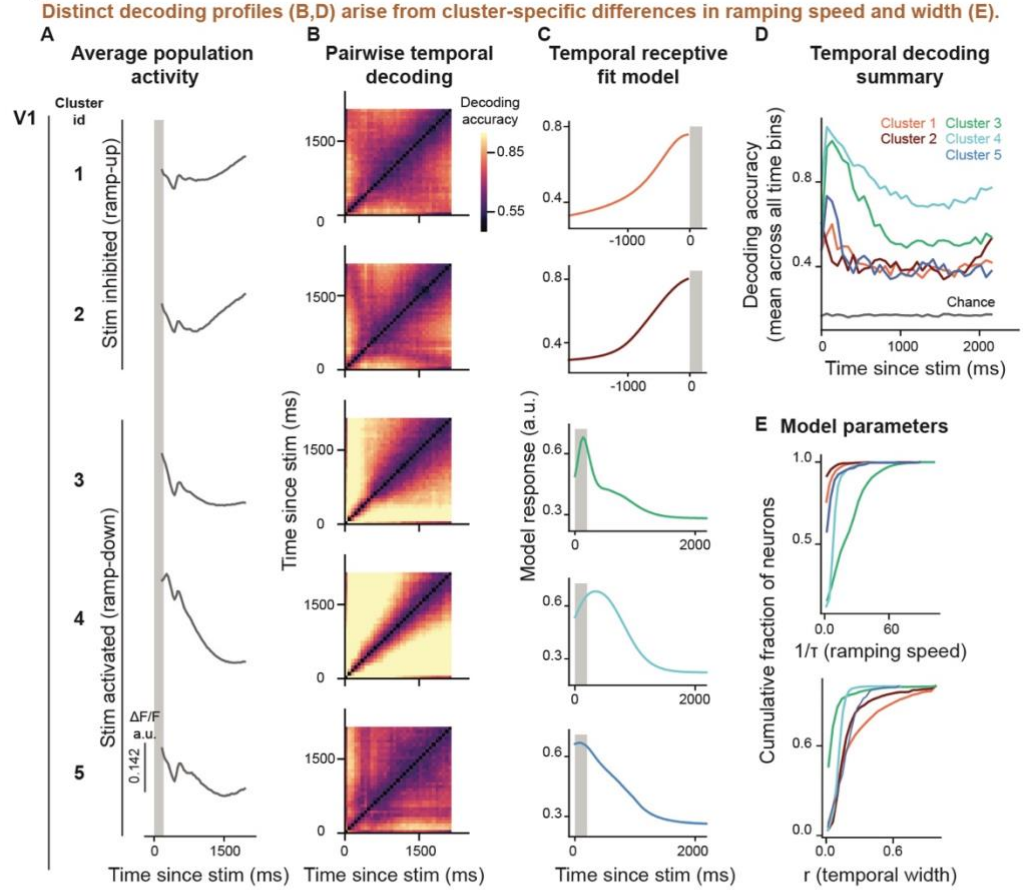

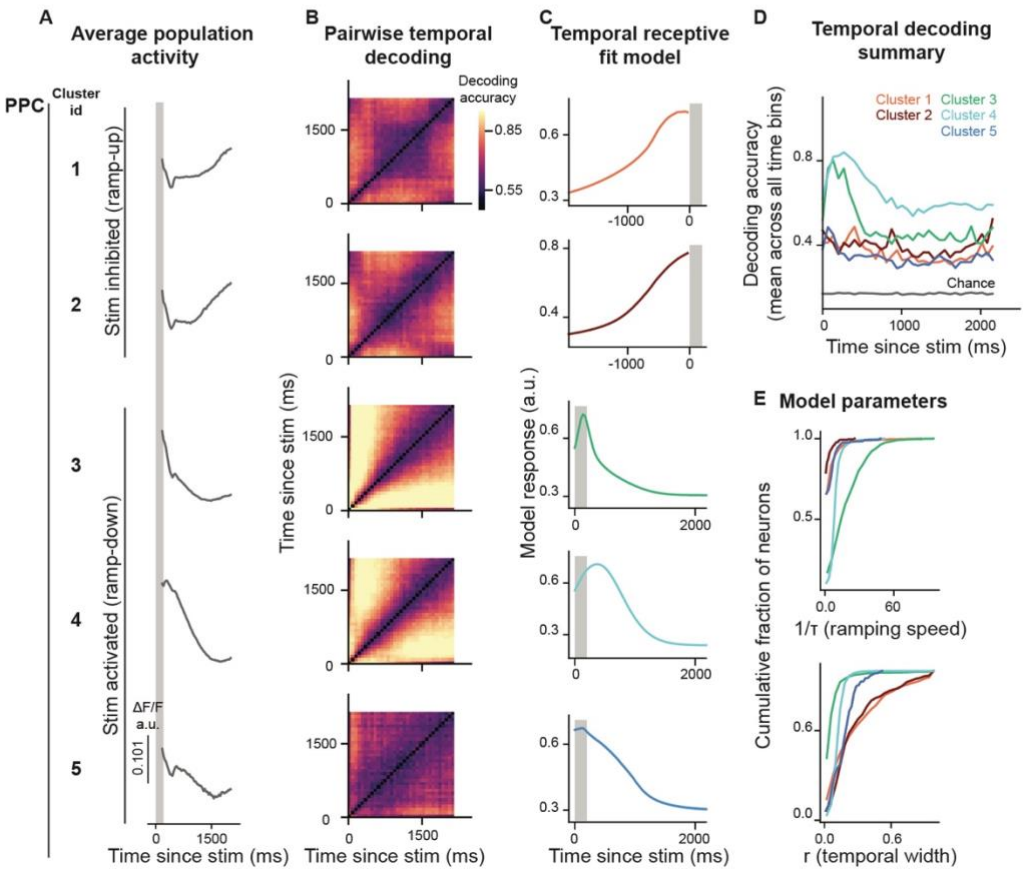

Figure 6. Heterogeneous rise/decay kinetics enable population coding of time.

Data from the long block of short/long sessions, showing heterogeneous kinetics across clusters, which leads to distinct temporal coding profiles across the interval. Clusters are the same as in Fig. 2. Each row corresponds to a cluster. **Top panels:** V1; **Bottom panels:** PPC.

A) Mean population activity, shown for each cluster (top to bottom).

B) Pairwise classification accuracy matrices (cross-validated). Each cell shows the accuracy for distinguishing a given pair of time bins, shown for each cluster. Cluster sizes were matched by neuron subsampling to enable cross-cluster comparison.

C) Temporal receptive field model response (see Fig. 1I), averaged across neurons, shown for each cluster. Orange, red: ramp-up clusters. Green, cyan, blue: ramp-down clusters.

D) Mean pairwise decoding accuracy at each time point, obtained by averaging panel B across all time bins, excluding the diagonal. Orange, red: ramp-up clusters. Green, blue, cyan: ramp-down clusters.

E) Distribution of model parameters across neurons within each cluster; Top: ramping speed ($1/\tau$); Bottom: temporal width (r). Distinct decoding profiles (B, D) arise from cluster-specific differences in ramping speed and temporal width.

Supplemental Figure 1

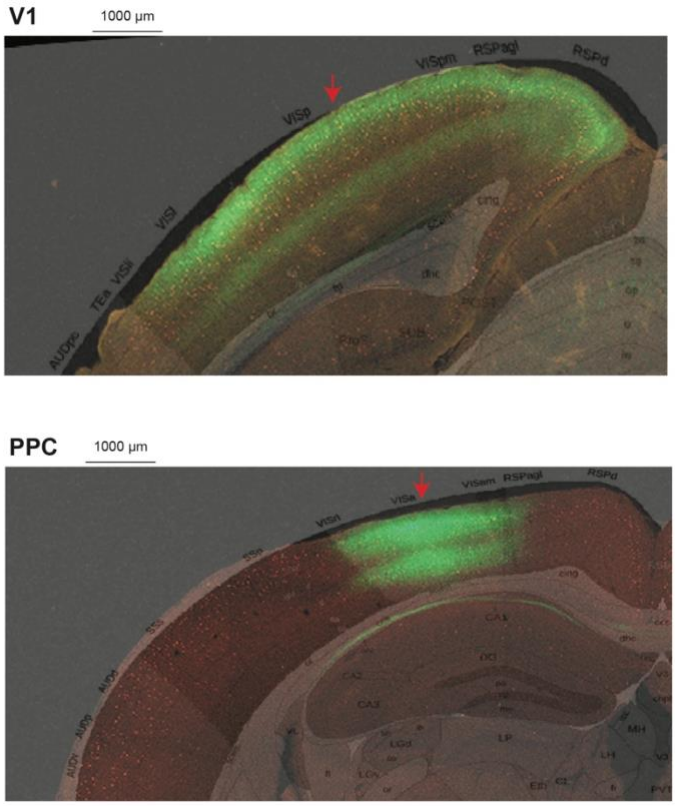

Supplemental Figure 1 (related to Fig. 1). Histological verification of imaging sites in visual and parietal cortex. Histology images from two example mice (VIP-tdTomato) imaged in V1 (**top**) or PPC (**bottom**), with Allen coronal slices superimposed. Red arrow: center of craniotomy window used for imaging, marking VISp (V1), and VISa (PPC). Green: cells labeled by GCaMP8f injection. Multiple injections were performed within the 3-mm cranial window. Two-photon imaging was primarily conducted from the window center.

Supplemental Figure 2

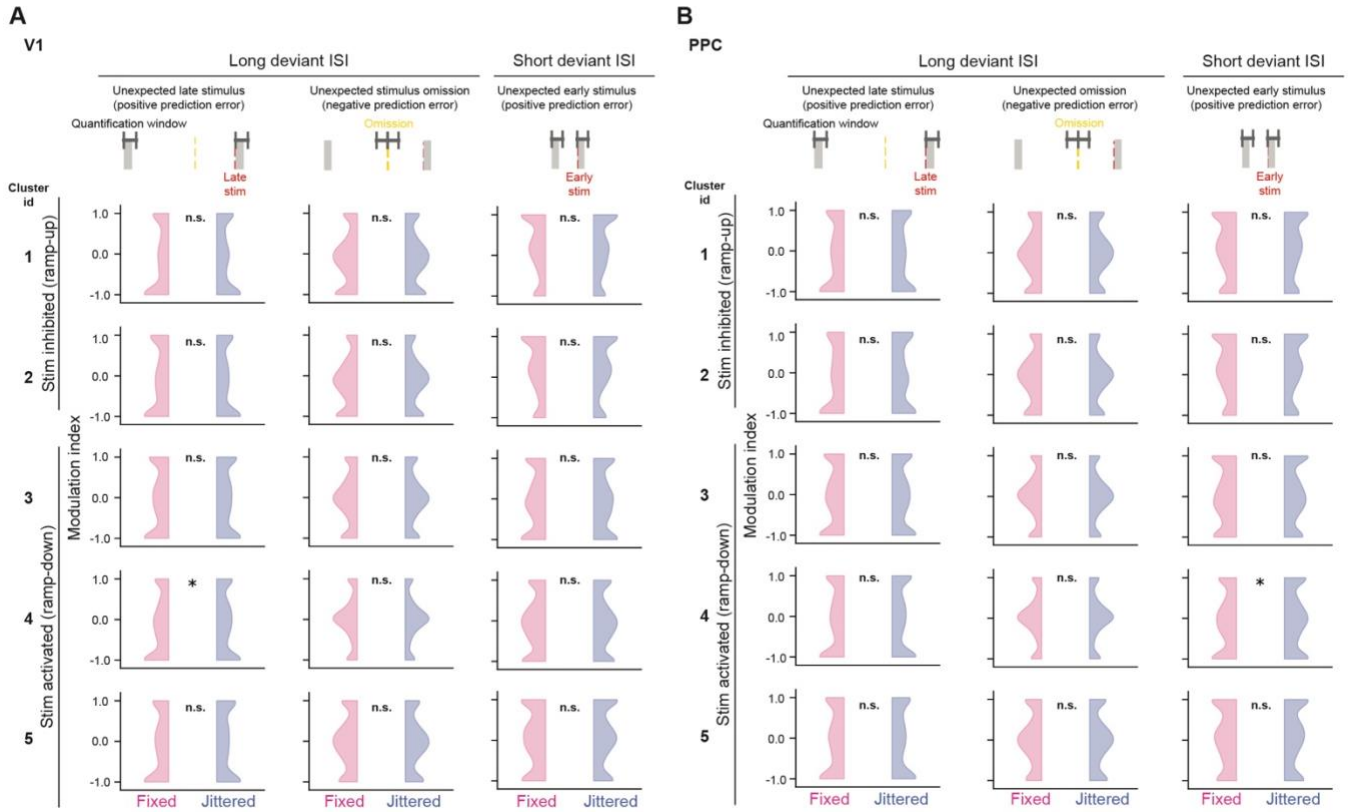

Supplemental Figure 2 (related to Fig. 4). Positive and negative prediction errors are represented similarly in fixed and jittered temporal contexts, ruling out temporal predictive processing as their underlying mechanism.

A) V1. **B)** PPC

Comparison of fixed (pink) and jittered (blue) block responses to unexpected events: late stimulus after a long deviant ISI (**left**, red line, positive prediction error), stimulus omission during a long deviant ISI (**middle**, yellow line, negative prediction error), and early stimulus after a short deviant ISI (**right**, red line, positive prediction error). Response modulation was quantified with a modulation index (Methods) by comparing neural activity across the two quantification windows (horizontal bars at the top, 300 ms each).

Supplemental Figure 3

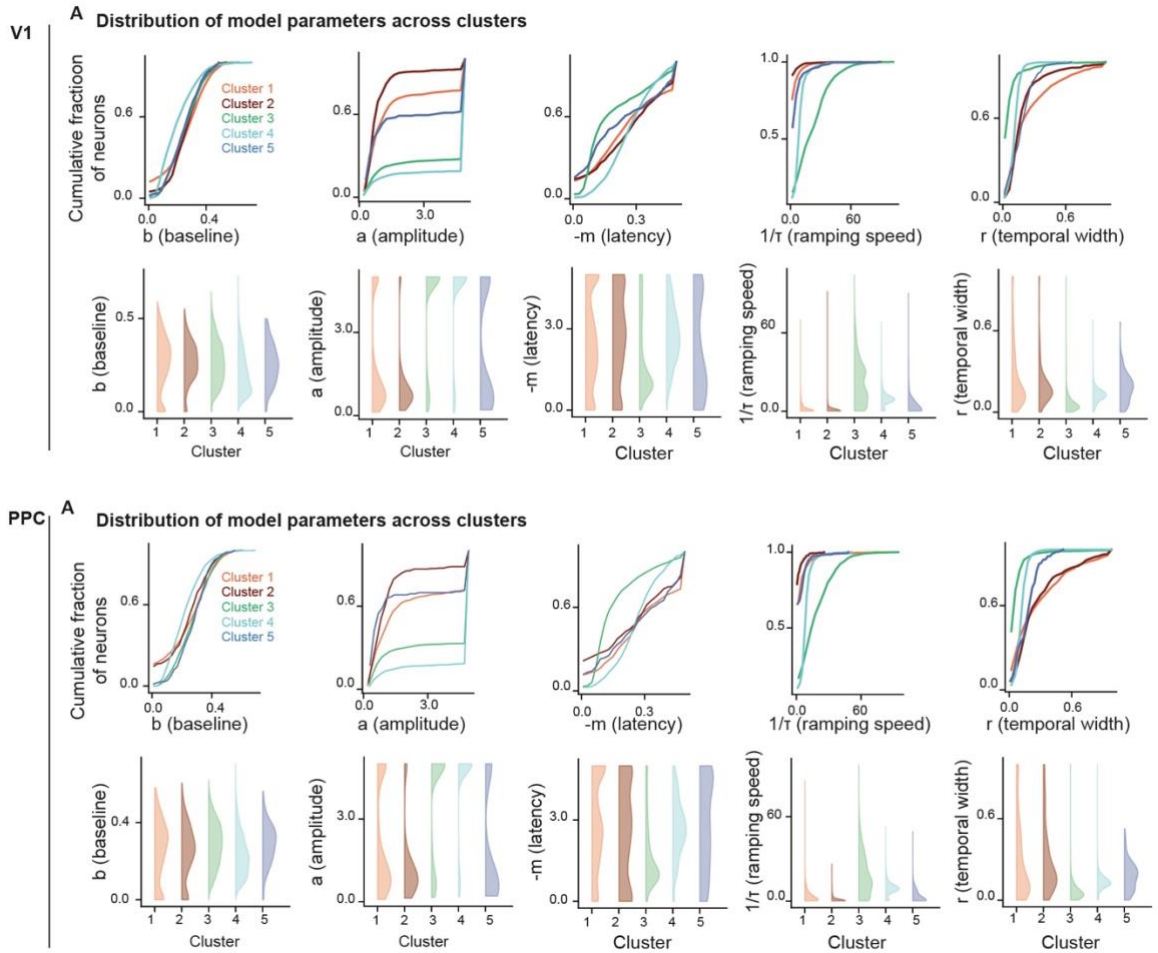

Supplemental Figure 3 (related to Fig. 6). Heterogeneous rise/decay kinetics enable population coding of time.

A) Comparison of the 5 parameters of the temporal receptive field model across all clusters (Orange, red: ramp-up clusters. Green, cyan, blue: ramp-down clusters). **Top:** cumulative histograms. **Bottom:** distributions.
'b' reflects the baseline shift and is similar across clusters since the activity is normalized.
'a' reflects the model response magnitude, which is bounded and clipped to avoid extreme values.
'm' reflects the time latency of activity peak, relative to stimulus onset.
'τ' is the time constant, reflecting the inverse of ramping speed.
'r' reflects the temporal width of the response.

References

Abbas, A. I., Sundiang, M. J. M., Henoch, B., Morton, M. P., Bolkan, S. S., Park, A. J., Harris, A. Z., Kellendonk, C., & Gordon, J. A. (2018). Somatostatin Interneurons Facilitate Hippocampal-Prefrontal Synchrony and Prefrontal Spatial Encoding. *Neuron*, *100*(4), 926-939.e923. https://doi.org/10.1016/j.neuron.2018.09.029

Abbott, L. F., & Regehr, W. G. (2004). Synaptic computation. *Nature*, *431*(7010), 796-803. https://doi.org/10.1038/nature03010

Abs, E., Poorthuis, R. B., Apelblat, D., Muhammad, K., Pardi, M. B., Enke, L., Kushinsky, D., Pu, D.-L., Eizinger, M. F., Conzelmann, K.-K., Spiegel, I., & Letzkus, J. J. (2018). Learning-Related Plasticity in Dendrite-Targeting Layer 1 Interneurons. *Neuron*, *100*(3), 684-699.e686. https://doi.org/https://doi.org/10.1016/j.neuron.2018.09.001

Adler, A., Zhao, R., Shin, M. E., Yasuda, R., & Gan, W. B. (2019). Somatostatin-Expressing Interneurons Enable and Maintain Learning-Dependent Sequential Activation of Pyramidal Neurons. *Neuron*, *102*(1), 202-216.e207. https://doi.org/10.1016/j.neuron.2019.01.036

Affan, R. O., Bright, I. M., Pemberton, L. N., Cruzado, N. A., Scott, B. B., & Howard, M. W. (2025). Ramping dynamics in the frontal cortex unfold over multiple timescales during motor planning. *Journal of Neurophysiology*, *133*(2), 625-637. https://doi.org/10.1152/jn.00234.2024

Aizenbud, I., Audette, N., Auksztulewicz, R., Basiński, K., Bastos, A. M., Berry, M., Canales-Johnson, A., Choi, H., Clopath, C., Cohen, U., Ponte Costa, R., De Filippo, R., Doronin, R., Errington, S. P., Gavornik, J. P., Gillon, C. J., Granier, A., Hamm, J. P., Hertäg, L.,...Sophy Xiong, Y. (2025). Neural mechanisms of predictive processing: a collaborative community experiment through the OpenScope program. arXiv:2504.09614. Retrieved April 01, 2025, from https://ui.adsabs.harvard.edu/abs/2025arXiv250409614A

Avanzini, P., Abdollahi, R. O., Sartori, I., Caruana, F., Pelliccia, V., Casaceli, G., Mai, R., Lo Russo, G., Rizzolatti, G., & Orban, G. A. (2016). Four-dimensional maps of the human somatosensory system. *Proc Natl Acad Sci U S A*, *113*(13), E1936-1943. https://doi.org/10.1073/pnas.1601889113

Barri, A., Wiechert, M. T., Jazayeri, M., & DiGregorio, D. A. (2022). Synaptic basis of a sub-second representation of time in a neural circuit model. *Nat Commun*, *13*(1), 7902. https://doi.org/10.1038/s41467-022-35395-y

Bastos, G., Holmes, J. T., Ross, J. M., Rader, A. M., Gallimore, C. G., Peterka, D. S., & Hamm, J. P. (2023). A frontosensory circuit for visual context processing is synchronous in the theta/alpha band. *bioRxiv*, 2023.2002.2025.530044. https://doi.org/10.1101/2023.02.25.530044

Bastos, G., Holmes, J. T., Ross, J. M., Rader, A. M., Gallimore, C. G., Wargo, J. A., Peterka, D. S., & Hamm, J. P. (2023). Top-down input modulates visual context processing through an interneuron-specific circuit. *Cell Rep*, *42*(9), 113133. https://doi.org/10.1016/j.celrep.2023.113133

Bernacchia, A., Seo, H., Lee, D., & Wang, X. J. (2011). A reservoir of time constants for memory traces in cortical neurons. *Nat Neurosci*, *14*(3), 366-372. https://doi.org/10.1038/nn.2752

Boven, E., Pickford, J., Apps, R., & Cerminara, N. L. (2025). Cerebellar involvement in self-timing. *bioRxiv*, 2025.2003.2005.641568. https://doi.org/10.1101/2025.03.05.641568

Breska, A., & Deouell, L. Y. (2017). Neural mechanisms of rhythm-based temporal prediction: Delta phase-locking reflects temporal predictability but not rhythmic entrainment. *PLOS Biology*, *15*(2), e2001665. https://doi.org/10.1371/journal.pbio.2001665

Bueti, D., & Walsh, V. (2009). The parietal cortex and the representation of time, space, number and other magnitudes. *Philos Trans R Soc Lond B Biol Sci*, *364*(1525), 1831-1840. https://doi.org/10.1098/rstb.2009.0028

Buonomano, D. V., & Maass, W. (2009). State-dependent computations: spatiotemporal processing in cortical networks. *Nat Rev Neurosci*, *10*(2), 113-125. https://doi.org/10.1038/nrn2558

Chabrol, F. P., Arenz, A., Wiechert, M. T., Margrie, T. W., & DiGregorio, D. A. (2015). Synaptic diversity enables temporal coding of coincident multisensory inputs in single neurons. *Nat Neurosci*, *18*(5), 718-727. https://doi.org/10.1038/nn.3974

Chubykin, A. A., Roach, E. B., Bear, M. F., & Shuler, M. G. (2013). A cholinergic mechanism for reward timing within primary visual cortex. *Neuron*, *77*(4), 723-735. https://doi.org/10.1016/j.neuron.2012.12.039

Churchland, M. M., Yu, B. M., Cunningham, J. P., Sugrue, L. P., Cohen, M. R., Corrado, G. S., Newsome, W. T., Clark, A. M., Hosseini, P., Scott, B. B., Bradley, D. C., Smith, M. A., Kohn, A., Movshon, J. A., Armstrong, K. M., Moore, T., Chang, S. W., Snyder, L. H., Lisberger, S. G.,...Shenoy, K. V. (2010). Stimulus onset quenches neural variability: a widespread cortical phenomenon. *Nature neuroscience*, *13*(3), 369-378. https://doi.org/10.1038/nn.2501

Cole, N., Harvey, M., Myers-Joseph, D., Gilra, A., & Khan, A. G. (2024). Prediction-error signals in anterior cingulate cortex drive task-switching. *Nature Communications*, *15*(1), 7088. https://doi.org/10.1038/s41467-024-51368-9

Coull, J. T., Cheng, R.-K., & Meck, W. H. (2011). Neuroanatomical and Neurochemical Substrates of Timing. *Neuropsychopharmacology*, *36*(1), 3-25. https://doi.org/10.1038/npp.2010.113

Cueva, C. J., Saez, A., Marcos, E., Genovesio, A., Jazayeri, M., Romo, R., Salzman, C. D., Shadlen, M. N., & Fusi, S. (2020). Low-dimensional dynamics for working memory and time encoding. *Proceedings of the National Academy of Sciences*, *117*(37), 23021-23032. https://doi.org/doi:10.1073/pnas.1915984117

Feldman, D. E. (2012). The spike-timing dependence of plasticity. *Neuron*, *75*(4), 556-571. https://doi.org/10.1016/j.neuron.2012.08.001

Fiser, A., Mahringer, D., Oyibo, H. K., Petersen, A. V., Leinweber, M., & Keller, G. B. (2016). Experience-dependent spatial expectations in mouse visual cortex. *Nat Neurosci*, *19*(12), 1658-1664. https://doi.org/10.1038/nn.4385

Friston, K., & Kiebel, S. (2009). Predictive coding under the free-energy principle. *Philos Trans R Soc Lond B Biol Sci*, *364*(1521), 1211-1221. https://doi.org/10.1098/rstb.2008.0300

Fu, Y., Kaneko, M., Tang, Y., Alvarez-Buylla, A., & Stryker, M. P. (2015). A cortical disinhibitory circuit for enhancing adult plasticity. *Elife*, *4*, e05558. https://doi.org/10.7554/eLife.05558

Furutachi, S., Franklin, A. D., Aldea, A. M., Mrsic-Flogel, T. D., & Hofer, S. B. (2024). Cooperative thalamocortical circuit mechanism for sensory prediction errors. *Nature*, *633*(8029), 398-406. https://doi.org/10.1038/s41586-024-07851-w

Gao, Z., Davis, C., Thomas, A. M., Economo, M. N., Abrego, A. M., Svoboda, K., De Zeeuw, C. I., & Li, N. (2018). A cortico-cerebellar loop for motor planning. *Nature*, *563*(7729), 113-116. https://doi.org/10.1038/s41586-018-0633-x

Garcia-Garcia, M. G., Kapoor, A., Akinwale, O., Takemaru, L., Kim, T. H., Paton, C., Litwin-Kumar, A., Schnitzer, M. J., Luo, L., & Wagner, M. J. (2024). A cerebellar granule cell-climbing fiber computation to learn to track long time intervals. *Neuron*, *112*(16), 2749-2764.e2747. https://doi.org/10.1016/j.neuron.2024.05.019

Garrett, M., Groblewski, P., Piet, A., Ollerenshaw, D., Najafi, F., Yavorska, I., Amster, A., Bennett, C., Buice, M., Caldejon, S., Casal, L., D'Orazi, F., Daniel, S., Vries, S. E. d., Kapner, D., Kiggins, J., Lecoq, J., Ledochowitsch, P., Manavi, S.,...Olsen, S. R. (2023). Stimulus novelty uncovers coding diversity in visual cortical circuits. *bioRxiv*, 2023.2002.2014.528085. https://doi.org/10.1101/2023.02.14.528085

Garrett, M., Groblewski, P., Piet, A., Ollerenshaw, D., Yavorska, I., Najafi, F., Amster, A., Bennett, C., Buice, M., Caldejon, S., Casal, L., D'Orazi, F., Daniel, S., de Vries, S. E., Kapner, D., Kiggins, J., Lecoq, J., Ledochowitsch, P., Manavi, S.,...Olsen, S. R. (2023). Stimulus novelty uncovers coding diversity in visual cortical circuits. *bioRxiv*, 2023.2002.2014.528085. https://doi.org/10.1101/2023.02.14.528085

Garrett, M., Manavi, S., Roll, K., Ollerenshaw, D. R., Groblewski, P. A., Ponvert, N. D., Kiggins, J. T., Casal, L., Mace, K., Williford, A., Leon, A., Jia, X., Ledochowitsch, P., Buice, M. A., Wakeman, W., Mihalas, S., & Olsen, S. R. (2020). Experience shapes activity dynamics and stimulus coding of VIP inhibitory cells. *Elife*, *9*. https://doi.org/10.7554/eLife.50340

Gavornik, J. P., & Bear, M. F. (2014). Learned spatiotemporal sequence recognition and prediction in primary visual cortex. *Nat Neurosci*, *17*(5), 732-737. https://doi.org/10.1038/nn.3683

Giovannucci, A., Badura, A., Deverett, B., Najafi, F., Pereira, T. D., Gao, Z., Ozden, I., Kloth, A. D., Pnevmatikakis, E., Paninski, L., De Zeeuw, C. I., Medina, J. F., & Wang, S. S. (2017). Cerebellar granule cells acquire a widespread predictive feedback signal during motor learning. *Nat Neurosci*, *20*(5), 727-734. https://doi.org/10.1038/nn.4531

Green, J., Bruno, C. A., Traunmüller, L., Ding, J., Hrvatin, S., Wilson, D. E., Khodadad, T., Samuels, J., Greenberg, M. E., & Harvey, C. D. (2023). A cell-type-specific error-correction signal in the posterior parietal cortex. *Nature*, *620*(7973), 366-373. https://doi.org/10.1038/s41586-023-06357-1

Hamm, J. P., Shymkiv, Y., Han, S., Yang, W., & Yuste, R. (2021). Cortical ensembles selective for context. *Proc Natl Acad Sci U S A*, *118*(14). https://doi.org/10.1073/pnas.2026179118

Harris, K. D., & Shepherd, G. M. G. (2015). The neocortical circuit: themes and variations. *Nature neuroscience*, *18*(2), 170-181. https://doi.org/10.1038/nn.3917

Hayashi, M. J., Ditye, T., Harada, T., Hashiguchi, M., Sadato, N., Carlson, S., Walsh, V., & Kanai, R. (2015). Time Adaptation Shows Duration Selectivity in the Human Parietal Cortex. *PLoS Biol*, *13*(9), e1002262. https://doi.org/10.1371/journal.pbio.1002262

Hennequin, G., Ahmadian, Y., Rubin, D. B., Lengyel, M., & Miller, K. D. (2018). The Dynamical Regime of Sensory Cortex: Stable Dynamics around a Single Stimulus-Tuned Attractor Account for Patterns of Noise Variability. *Neuron*, *98*(4), 846-860.e845. https://doi.org/https://doi.org/10.1016/j.neuron.2018.04.017

Hertäg, L., & Sprekeler, H. (2020). Learning prediction error neurons in a canonical interneuron circuit. *Elife*, *9*, e57541. https://doi.org/10.7554/eLife.57541

Herzfeld, D. J., & Lisberger, S. G. (2025). Neural circuit mechanisms to transform cerebellar population dynamics for motor control in monkeys. *bioRxiv*. https://doi.org/10.1101/2025.02.21.639459

Hockley, A., Bohórquez, L. H., & Malmierca, M. S. (2025). Top-down prediction signals from the medial prefrontal cortex govern auditory cortex prediction errors. *Cell Rep*, *44*(4), 115538. https://doi.org/10.1016/j.celrep.2025.115538

Hodgkin, A. L., & Huxley, A. F. (1952). A quantitative description of membrane current and its application to conduction and excitation in nerve. *J Physiol*, *117*(4), 500-544. https://doi.org/10.1113/jphysiol.1952.sp004764

Ibrahim, L. A., Huang, S., Fernandez-Otero, M., Sherer, M., Qiu, Y., Vemuri, S., Xu, Q., Machold, R., Pouchelon, G., Rudy, B., & Fishell, G. (2021). Bottom-up inputs are required for establishment of top-down connectivity onto cortical layer 1 neurogliaform cells. *Neuron*, *109*(21), 3473-3485.e3475. https://doi.org/https://doi.org/10.1016/j.neuron.2021.08.004

Inagaki, H. K., Fontolan, L., Romani, S., & Svoboda, K. (2019). Discrete attractor dynamics underlies persistent activity in the frontal cortex. *Nature*, *566*(7743), 212-217. https://doi.org/10.1038/s41586-019-0919-7

Janssen, P., & Shadlen, M. N. (2005). A representation of the hazard rate of elapsed time in macaque area LIP. *Nat Neurosci*, *8*(2), 234-241. https://doi.org/10.1038/nn1386

Jaramillo, S., & Zador, A. M. (2011). The auditory cortex mediates the perceptual effects of acoustic temporal expectation. *Nat Neurosci*, *14*(2), 246-251. https://doi.org/10.1038/nn.2688

Jordan, R., & Keller, G. B. (2020). Opposing influence of top-down and bottom-up input on different types of excitatory layer 2/3 neurons in mouse visual cortex. *bioRxiv*.

Kameda, M., Ohmae, S., & Tanaka, M. (2019). Entrained neuronal activity to periodic visual stimuli in the primate striatum compared with the cerebellum. *Elife*, *8*, e48702. https://doi.org/10.7554/eLife.48702

Keller, A. J., Roth, M. M., & Scanziani, M. (2020). Feedback generates a second receptive field in neurons of the visual cortex. *Nature*, *582*(7813), 545-549. https://doi.org/10.1038/s41586-020-2319-4

Keller, G. B., & Mrsic-Flogel, T. D. (2018). Predictive Processing: A Canonical Cortical Computation. *Neuron*, *100*(2), 424-435. https://doi.org/10.1016/j.neuron.2018.10.003

Kim, J., Ghim, J.-W., Lee, J. H., & Jung, M. W. (2013). Neural Correlates of Interval Timing in Rodent Prefrontal Cortex. *The Journal of Neuroscience*, *33*(34), 13834-13847. https://doi.org/10.1523/jneurosci.1443-13.2013

Laje, R., & Buonomano, D. V. (2013). Robust timing and motor patterns by taming chaos in recurrent neural networks. *Nat Neurosci*, *16*(7), 925-933. https://doi.org/10.1038/nn.3405

Leon, M. I., & Shadlen, M. N. (2003). Representation of time by neurons in the posterior parietal cortex of the macaque. *Neuron*, *38*(2), 317-327. https://doi.org/10.1016/s0896-6273(03)00185-5

MacDonald, C. J., Lepage, K. Q., Eden, U. T., & Eichenbaum, H. (2011). Hippocampal "time cells" bridge the gap in memory for discontiguous events. *Neuron*, *71*(4), 737-749. https://doi.org/10.1016/j.neuron.2011.07.012

Machens, C. K., Romo, R., & Brody, C. D. (2010). Functional, But Not Anatomical, Separation of “What” and “When” in Prefrontal Cortex. *The Journal of Neuroscience*, *30*(1), 350-360. https://doi.org/10.1523/jneurosci.3276-09.2010

Mante, V., Sussillo, D., Shenoy, K. V., & Newsome, W. T. (2013). Context-dependent computation by recurrent dynamics in prefrontal cortex. *Nature*, *503*(7474), 78-84. https://doi.org/10.1038/nature12742

Marder, E., & Goaillard, J. M. (2006). Variability, compensation and homeostasis in neuron and network function. *Nat Rev Neurosci*, *7*(7), 563-574. https://doi.org/10.1038/nrn1949

Maristany de las Casas, E., Killmann, K., Drüke, M., Münster, L., Ebner, C., Sachdev, R., Jaeger, D., & Larkum, M. E. (2025). Tuft dendrites in frontal motor cortex enable flexible learning. *bioRxiv*, 2025.2003.2013.642781. https://doi.org/10.1101/2025.03.13.642781

Matell, M. S., Meck, W. H., & Nicolelis, M. A. (2003). Interval timing and the encoding of signal duration by ensembles of cortical and striatal neurons. *Behav Neurosci*, *117*(4), 760-773. https://doi.org/10.1037/0735-7044.117.4.760

Medina, J. F., & Mauk, M. D. (2000). Computer simulation of cerebellar information processing. *Nat Neurosci*, *3 Suppl*, 1205-1211. https://doi.org/10.1038/81486

Mello, G. B., Soares, S., & Paton, J. J. (2015). A scalable population code for time in the striatum. *Curr Biol*, *25*(9), 1113-1122. https://doi.org/10.1016/j.cub.2015.02.036

Moberget, T., Karns, C. M., Deouell, L. Y., Lindgren, M., Knight, R. T., & Ivry, R. B. (2008). Detecting violations of sensory expectancies following cerebellar degeneration: a mismatch negativity study. *Neuropsychologia*, *46*(10), 2569-2579. https://doi.org/10.1016/j.neuropsychologia.2008.03.016

Murray, J. D., Bernacchia, A., Freedman, D. J., Romo, R., Wallis, J. D., Cai, X., Padoa-Schioppa, C., Pasternak, T., Seo, H., Lee, D., & Wang, X.-J. (2014). A hierarchy of intrinsic timescales across primate cortex. *Nature neuroscience*, *17*(12), 1661-1663. https://doi.org/10.1038/nn.3862

Najafi, F., Elsayed, G. F., Cao, R., Pnevmatikakis, E., Latham, P. E., Cunningham, J. P., & Churchland, A. K. (2020). Excitatory and Inhibitory Subnetworks Are Equally Selective during Decision-Making and Emerge Simultaneously during Learning. *Neuron*, *105*(1), 165-179 e168. https://doi.org/10.1016/j.neuron.2019.09.045

Najafi, F., Giovannucci, A., Wang, S. S., & Medina, J. F. (2014). Sensory-driven enhancement of calcium signals in individual Purkinje cell dendrites of awake mice. *Cell Rep*, *6*(5), 792-798. https://doi.org/10.1016/j.celrep.2014.02.001

Najafi, F., & Medina, J. F. (2013). Beyond "all-or-nothing" climbing fibers: graded representation of teaching signals in Purkinje cells. *Front Neural Circuits*, *7*, 115. https://doi.org/10.3389/fncir.2013.00115

Najafi, F., Russo, S., & Lecoq, J. (2025). Unexpected events trigger task-independent signaling in VIP and excitatory neurons of mouse visual cortex. *iScience*, *28*(2), 111728. https://doi.org/10.1016/j.isci.2024.111728

Narayanan, N. S. (2016). Ramping activity is a cortical mechanism of temporal control of action. *Curr Opin Behav Sci*, *8*, 226-230. https://doi.org/10.1016/j.cobeha.2016.02.017

Nitzan, N., & Buzsáki, G. (2025). Diversity of omission responses to visual images across brain-wide regions. *Sci Adv*, *11*(21), eadv5651. https://doi.org/10.1126/sciadv.adv5651

O'Reilly, J. X., Mesulam, M. M., & Nobre, A. C. (2008). The cerebellum predicts the timing of perceptual events. *J Neurosci*, *28*(9), 2252-2260. https://doi.org/10.1523/jneurosci.2742-07.2008

Ohmae, S., Kunimatsu, J., & Tanaka, M. (2017). Cerebellar Roles in Self-Timing for Sub- and Supra-Second Intervals. *J Neurosci*, *37*(13), 3511-3522. https://doi.org/10.1523/jneurosci.2221-16.2017

Pachitariu, M., Stringer, C., Dipoppa, M., Schröder, S., Rossi, L. F., Dalgleish, H., Carandini, M., & Harris, K. D. (2017). Suite2p: beyond 10,000 neurons with standard two-photon microscopy. *bioRxiv*, 061507. https://doi.org/10.1101/061507

Pastalkova, E., Itskov, V., Amarasingham, A., & Buzsáki, G. (2008). Internally generated cell assembly sequences in the rat hippocampus. *Science*, *321*(5894), 1322-1327. https://doi.org/10.1126/science.1159775

Paton, J. J., & Buonomano, D. V. (2018). The Neural Basis of Timing: Distributed Mechanisms for Diverse Functions. *Neuron*, *98*(4), 687-705. https://doi.org/10.1016/j.neuron.2018.03.045

Pi, H.-J., Hangya, B., Kvitsiani, D., Sanders, J. I., Huang, Z. J., & Kepecs, A. (2013). Cortical interneurons that specialize in disinhibitory control. *Nature*, *503*(7477), 521-524. https://doi.org/10.1038/nature12676

Rajan, K., Abbott, L. F., & Sompolinsky, H. (2010). Stimulus-dependent suppression of chaos in recurrent neural networks. *Physical Review E*, *82*(1), 011903. https://doi.org/10.1103/PhysRevE.82.011903

Rao, R. P., & Ballard, D. H. (1999). Predictive coding in the visual cortex: a functional interpretation of some extra-classical receptive-field effects. *Nat Neurosci*, *2*(1), 79-87. https://doi.org/10.1038/4580

Sara, S. J., & Bouret, S. (2012). Orienting and reorienting: the locus coeruleus mediates cognition through arousal. *Neuron*, *76*(1), 130-141. https://doi.org/10.1016/j.neuron.2012.09.011

Schneider, B. A., & Ghose, G. M. (2012). Temporal production signals in parietal cortex. *PLoS Biol*, *10*(10), e1001413. https://doi.org/10.1371/journal.pbio.1001413

Schneider, D. M., Sundararajan, J., & Mooney, R. (2018). A cortical filter that learns to suppress the acoustic consequences of movement. *Nature*, *561*(7723), 391-395. https://doi.org/10.1038/s41586-018-0520-5

Seamans, J. K., & Yang, C. R. (2004). The principal features and mechanisms of dopamine modulation in the prefrontal cortex. *Prog Neurobiol*, *74*(1), 1-58. https://doi.org/10.1016/j.pneurobio.2004.05.006

Shadmehr, R., Smith, M. A., & Krakauer, J. W. (2010). Error correction, sensory prediction, and adaptation in motor control. *Annu Rev Neurosci*, *33*, 89-108. https://doi.org/10.1146/annurev-neuro-060909-153135

Shin, H., & Adesnik, H. (2021). NDNF interneurons, Spartans of the cortical column: Small in number, strong in impact. *Neuron*, *109*(13), 2041-2042. https://doi.org/https://doi.org/10.1016/j.neuron.2021.06.022

Shuler, M. G., & Bear, M. F. (2006). Reward timing in the primary visual cortex. *Science*, *311*(5767), 1606-1609. https://doi.org/10.1126/science.1123513

Steinmetz, N. A., Zatka-Haas, P., Carandini, M., & Harris, K. D. (2019). Distributed coding of choice, action and engagement across the mouse brain. *Nature*, *576*(7786), 266-273. https://doi.org/10.1038/s41586-019-1787-x

Stringer, C., & Pachitariu, M. (2025). Cellpose3: one-click image restoration for improved cellular segmentation. *Nature Methods*, *22*(3), 592-599. https://doi.org/10.1038/s41592-025-02595-5

Suvrathan, A., Payne, H. L., & Raymond, J. L. (2016). Timing Rules for Synaptic Plasticity Matched to Behavioral Function. *Neuron*, *92*(5), 959-967. https://doi.org/10.1016/j.neuron.2016.10.022

Szadai, Z., Pi, H. J., Chevy, Q., Ócsai, K., Albeanu, D. F., Chiovini, B., Szalay, G., Katona, G., Kepecs, A., & Rózsa, B. (2022). Cortex-wide response mode of VIP-expressing inhibitory neurons by reward and punishment. *Elife*, *11*. https://doi.org/10.7554/eLife.78815

Tesche, C. D., & Karhu, J. J. (2000). Anticipatory cerebellar responses during somatosensory omission in man. *Hum Brain Mapp*, *9*(3), 119-142. https://doi.org/10.1002/(SICI)1097-0193(200003)9:3<119::AID-HBM2>3.0.CO;2-R

Tremblay, R., Lee, S., & Rudy, B. (2016). GABAergic Interneurons in the Neocortex: From Cellular Properties to Circuits. *Neuron*, *91*(2), 260-292. https://doi.org/10.1016/j.neuron.2016.06.033

Tsao, A., Yousefzadeh, S. A., Meck, W. H., Moser, M. B., & Moser, E. I. (2022). The neural bases for timing of durations. *Nat Rev Neurosci*, *23*(11), 646-665. https://doi.org/10.1038/s41583-022-00623-3

Van Derveer, A. B., Ross, J. M., & Hamm, J. P. (2023). Robust multisensory deviance detection in the mouse parietal associative area. *Curr Biol*, *33*(18), 3969-3976.e3964. https://doi.org/10.1016/j.cub.2023.08.002

Vélez-Fort, M., Rousseau, C. V., Niedworok, C. J., Wickersham, I. R., Rancz, E. A., Brown, A. P., Strom, M., & Margrie, T. W. (2014). The stimulus selectivity and connectivity of layer six principal cells reveals cortical microcircuits underlying visual processing. *Neuron*, *83*(6), 1431-1443. https://doi.org/10.1016/j.neuron.2014.08.001

Wang, J., Narain, D., Hosseini, E. A., & Jazayeri, M. (2018). Flexible timing by temporal scaling of cortical responses. *Nature neuroscience*, *21*(1), 102-110. https://doi.org/10.1038/s41593-017-0028-6

Wang, S., Falcone, R., Richmond, B., & Averbeck, B. B. (2023). Attractor dynamics reflect decision confidence in macaque prefrontal cortex. *Nat Neurosci*, *26*(11), 1970-1980. https://doi.org/10.1038/s41593-023-01445-x

Wang, X.-J. (2008). Decision Making in Recurrent Neuronal Circuits. *Neuron*, *60*(2), 215-234. https://doi.org/10.1016/j.neuron.2008.09.034

Wang, X. J. (2008). Decision making in recurrent neuronal circuits. *Neuron*, *60*(2), 215-234. https://doi.org/10.1016/j.neuron.2008.09.034

Wei, Z., Lin, B.-J., Chen, T.-W., Daie, K., Svoboda, K., & Druckmann, S. (2020). A comparison of neuronal population dynamics measured with calcium imaging and electrophysiology. *PLOS Computational Biology*, *16*(9), e1008198. https://doi.org/10.1371/journal.pcbi.1008198

Xu, M., Zhang, S. Y., Dan, Y., & Poo, M. M. (2014). Representation of interval timing by temporally scalable firing patterns in rat prefrontal cortex. *Proc Natl Acad Sci U S A*, *111*(1), 480-485. https://doi.org/10.1073/pnas.1321314111

Yaron, A., Shiramatsu-Isoguchi, T., Kern, F. B., Ohki, K., Takahashi, H., & Chao, Z. C. (2024). Omission-responsive neurons encode negative prediction error and probability in the auditory cortex. *bioRxiv*, 2024.2009.2009.612166. https://doi.org/10.1101/2024.09.09.612166

Zhang, Y., Rózsa, M., Liang, Y., Bushey, D., Wei, Z., Zheng, J., Reep, D., Broussard, G. J., Tsang, A., Tsegaye, G., Narayan, S., Obara, C. J., Lim, J.-X., Patel, R., Zhang, R., Ahrens, M. B., Turner, G. C., Wang, S. S. H., Korff, W. L.,...Looger, L. L. (2023). Fast and sensitive GCaMP calcium indicators for imaging neural populations. *Nature*, *615*(7954), 884-891. https://doi.org/10.1038/s41586-023-05828-9

Zhou, S., Masmanidis, S. C., & Buonomano, D. V. (2020). Neural Sequences as an Optimal Dynamical Regime for the Readout of Time. *Neuron*, *108*(4), 651-658.e655. https://doi.org/10.1016/j.neuron.2020.08.020

Zhou, Z. C., Huang, W. A., Yu, Y., Negahbani, E., Stitt, I. M., Alexander, M. L., Hamm, J. P., Kato, H. K., & Fröhlich, F. (2020). Stimulus-specific regulation of visual oddball differentiation in posterior parietal cortex. *Sci Rep*, *10*(1), 13973. https://doi.org/10.1038/s41598-020-70448-6

Zhuang, J., Ng, L., Williams, D., Valley, M., Li, Y., Garrett, M., & Waters, J. (2017). An extended retinotopic map of mouse cortex. *Elife*, *6*, e18372. https://doi.org/10.7554/eLife.18372

Zucker, R. S., & Regehr, W. G. (2002). Short-term synaptic plasticity. *Annu Rev Physiol*, *64*, 355-405. https://doi.org/10.1146/annurev.physiol.64.092501.114547